공학박사 학위논문

Smartphone based micro-endoscopic devices development for pre-clinical, clinical applications, and data quantification of *in vivo* endoscopic image

전임상 및 임상 활용을 위한 스마트폰 기반 내시현미경 장비 개발과 생체 내시경 영상 데이터 정량화

울 산 대 학 교 대 학 원

의 과 학 과

김 영 규

Smartphone based micro-endoscopic devices development for pre-clinical, clinical applications, and data quantification of *in vivo* endoscopic image

지도교수 김 준 기

이 논문을 공학박사 학위 논문으로 제출함

2023년 08월

울 산 대 학 교 대 학 원

의 과 학 과

김 영 규

김영규의 공학박사학위 논문을 인준함

심사위원 백 찬 기 (인)

심사위원 문 영 진 (인)

심사위원 이 윤 세 (인)

심사위원 최 우 준 (인)

심사위원 김 준 기 (인)

울 산 대 학 교 대 학 원

2023년 08월

Abstract

In the field of clinical diagnosis, endoscopy is a unique diagnostic tool that allows for obtaining optical images of various internal organs in the human body. Since the introduction of endoscopy in clinical practice, its importance and utility in clinical diagnosis have steadily increased along with the improvement of endoscopic performance. Due to the clinical significance of endoscopy, there have been attempts to apply endoscopy in the field of point-of-care testing (POCT), which is highly regarded in the medical field. Additionally, smartphones are considered one of the most important devices in the field of point-of-care testing due to their significant advancements in performance, portability, and widespread use. Given the importance of endoscopy and point-of-care testing, smartphones have been utilized as essential tools for the integration of endoscopy into point-of-care testing, and this study aimed to explore the possibility of acquiring endoscopic images using smartphones and utilizing them in the field of clinical diagnosis.

In the first study, we conducted research to investigate whether endoscopic images of vocal fold vibrations could be obtained using a smartphone's camera and whether they could be used for image-based diagnosis. To acquire images of vocal fold vibrations, we utilized the high-speed shooting function of smartphones and used a self-developed endoscopic smartphone adapter to obtain actual clinical videos of vocal fold vibrations from four patients with different pathologies, in addition to normal subjects. The acquired clinical videos of vocal fold vibrations were quantified through image processing analysis, and the comparison of quantified variables demonstrated not only the distinction between normal subjects and patients but also the differentiation between pathologies in patients.

In the following study, aiming to enhance the diagnostic potential of smartphone-based endoscopic images as revealed in previous research, we sought to obtain functional images rather than mere laryngeal endoscopic images. We employed laser speckle contrast imaging

(LSCI) analysis to achieve this. To implement LSCI, we developed an endoscopic smartphone adapter with additional components and verified its functionality through a phantom mimicking biological tissue. To prove that the validated equipment for LSCI analysis can be used in actual *in vivo* imaging, we acquired vascular images within the bladder of mice and demonstrated the differences in vascular images between mice with bladder cancer induction and normal mice through LSCI analysis.

As a final subsequent study, in addition to the analysis of LSCI developed in the previous research, we aimed to obtain diffuse reflectance imaging (DRI) to confirm tissue blood flow and the possibility of tissue damage caused by changes in oxygen saturation. To implement both LSCI and DRI, we used an RGB laser module, and similar to the validation method for LSCI, we used a phantom mimicking biological tissue to verify the capability of LSCI analysis. Furthermore, we conducted experiments involving the occlusion of mesenteric vessels in mice to verify the acquisition of tissue oxygen saturation images using DRI. By successfully implementing both LSCI and DRI in a smartphone-based endoscopic device, the possibility of using smartphone-based endoscopic imaging devices in actual clinical settings was further enhanced.

Contents

List of Figures

List of Tables

Introduction

Since the announcement of the clinical feasibility of the first endoscope using a candle, mirror, and tin tube by Germany's Philip Bozzini in 1805 [1], the rigid endoscope using a metal tube was developed by Adolf Kussmaul in 1868. Subsequently, in 1932, Germany's Rudolf Schindler developed a basic form of a flexible endoscope with a bending section capable of bending up to 30 degrees using multiple lenses, which began to be widely used in clinical settings. In 1958, Basil Hirschowitz from the United States developed a flexible endoscope made of optical fibers, ushering in the era of clinical medical endoscopes [2]. These flexible endoscopes allowed for access to more organs, and in 1983, Welch-Allyn produced the first electronic endoscope or video endoscope using a CCD (Charged Coupled Device), overcoming the limitations of image resolution that previous flexible endoscopes had, enabling more in-depth image processing and analysis [3].

Today, endoscopic imaging has undergone significant advancements due to innovations in cutting-edge semiconductor technology, becoming an essential tool for primary diagnosis, treatment, and surgery in modern clinical practice. Endoscopes remain the easiest imaging equipment for visualizing internal organs, such as the digestive system, among various medical imaging devices. Unlike in the past, when endoscopes were used only for diagnosis, they now play a unique role in not only diagnosis but also biopsy and minimally invasive surgeries such as robotic surgery and laparoscopic surgery.[4-9] In the area of image diagnostics, a basic function of endoscopes, they now provide functional imaging, such as narrow-band imaging (NBI) and dye-based chromoendoscopy (DBCE), enabling diagnoses that were previously impossible with conventional endoscopes.[10]

The advancements in endoscopic imaging have also been applied to image analysis using AI and machine learning, which are gaining widespread attention. Research on image analysis is actively being conducted, and the importance of endoscopes in clinical settings is expected to continue to grow in the future.[11]

Due to the solid utilization of endoscopes as clinical diagnostic tools in hospitals, the demand for endoscopes for point-of-care testing (POCT) is also gradually increasing. [12-14] POCT refers to a diagnostic testing method performed at the patient's location rather than the patient traveling to a medical facility such as a hospital to receive tests. This approach enables rapid and cost-effective diagnosis on-site without sending samples to a hospital or having the patient travel. Consequently, POCT is receiving increasing attention as a solution for areas with limited access to medical facilities, such as developing countries, where patients' residences and hospitals may be far apart. Since current clinical endoscopes require peripheral devices such as power supply units, data processing units, and image display devices, they are not suitable for field diagnostics without miniaturizing these devices. With the advancement of electronic devices, portable endoscope systems have been developed and initially used in veterinary medicine for examining animal body cavities[15, 16] and diagnosing the gastrointestinal tracts of clinical patients[17, 18]. However, these portable endoscope systems still weigh 8-9 kg, making them difficult to carry, and their prices are too high for mass adoption. This highlights the need to develop smaller, lightweight, easy-to-use, and more affordable POCT endoscope systems for individual use.

To develop more compact and cost-effective endoscope equipment for POCT applications, the focus has shifted to smartphones, which are widely owned by individuals. Over the past 20 years, smartphones have demonstrated unparalleled advancements in the fields of mobile computing and communication since their inception. While smartphones have achieved tremendous progress in their processing processors and other sensors, the camera technology integrated into smartphones can be considered one of the most competitively and innovatively focused areas among various smartphone manufacturers.[19-23] Due to such competition and innovation, the current camera performance of smartphones typically supports the acquisition of up to 60fps video at 2160p resolution using high-resolution CMOS sensors. Additionally, at lower resolutions such as 720p or 1080p, smartphones now support the capture of ultra-high-speed video at 120 to 960fps.[24]

Due to the aforementioned advancements in smartphone performance, their applications are being extended into medical Point-Of-Care devices.[25, 26] With their powerful processors and camera performance, most smartphone-based Point-Of-Care devices are heavily centered around camera function. To develop a smartphone-based Point-Of-Care Testing (POCT) device that can be effectively used as a diagnostic tool in clinical settings,[27-30] we attempted to integrate the rapidly advancing smartphone camera sensor with clinical endoscopic equipment. To this end, we developed a basic device that combines a smartphone and an endoscope, enabling the acquisition of endoscopic images through the smartphone's built-in camera sensor. We aimed to first confirm the clinical diagnostic feasibility by utilizing the developed device and the high-speed image acquisition function of the smartphone camera. Furthermore, since obtaining not only bright-field images but also functional images in clinical endoscopy can enhance the scope and accuracy of diagnosis through endoscopic images, we

explored ways to apply this within the bounds of the developed smartphone-endoscope combined device for POCT. Consequently, we attempted to apply the Laser Speckle Contrast Imaging (LSCI) and Diffuse Reflectance Imaging (DRI) image analysis techniques.

These two image analysis techniques were found to be compatible with the intended smartphone-based POCT device,[31, 32] as they allowed for image acquisition and analysis with the simple addition of a laser light source. We first confirmed that LSCI images could be obtained by applying a single laser light source to the flexible endoscope. Subsequently, using an RGB laser module, we acquired both LSCI and DRI images, enabling the capture of not only simple bright-field morphological images but also functional images of blood flow changes and tissue oxygen saturation changes. This confirmed the potential usability of the smartphone-based endoscope POCT device as a more conclusively diagnostic tool in clinical settings.

In this study, we aimed to develop a smartphone-based endoscope for POCT that can effectively serve as a diagnostic device in clinical settings. We combined a rapidly advancing smartphone camera sensor with clinical endoscopic equipment and developed a basic device capable of acquiring endoscopic images through the smartphone's built-in camera sensor. We assessed the clinical diagnostic feasibility by utilizing the developed device and the high-speed image acquisition function of the smartphone camera. Furthermore, we explored ways to apply LSCI and DRI techniques, which can enhance the scope and accuracy of diagnosis through endoscopic images. We found that these two image analysis techniques allowed for image acquisition and analysis with the simple addition of a laser light source, confirming their

compatibility with the intended smartphone-based POCT device. Our results demonstrated the potential usability of the smartphone-based endoscope POCT device as a diagnostic tool in clinical settings

Principle

Laser speckle contrast imaging (LSCI)

Laser Speckle Contrast Imaging (LSCI) was first utilized in the biomedical field in 1981 by Fercher and Biers.[33] LSCI is a highly promising imaging analysis method in medical imaging due to its advantage of quickly acquiring perfusion mapping images over a wide imaging area with a simple and inexpensive configuration.[34-36] In the 1980s, when LSCI was first applied to the field of biomedicine, it was difficult to use in actual clinical practice due to the limitations of analog systems and non-real-time analysis methods. However, with the development of computer systems enabling high-speed image processing and the low-power, low-cost mass production of laser diodes as essential components, real-time LSCI analysis has become possible even with low-cost system configurations, greatly increasing its potential for clinical application.[37-39]

Speckle patterns used in LSCI analysis refer to random interference patterns created when coherent light from a laser source is scattered by a scattering medium in biological tissue. The optical path of the light differs at each point of the image due to the scattering medium in the biological tissue, causing light to reach the camera sensor at random mutual phases, resulting in an interference pattern composed of bright and dark spots. These speckle patterns can be classified into two types: static speckles and dynamic speckles. Static speckles do not change over time because the scattering medium does not change. Dynamic speckles change over time due to changes in the scattering medium, such as movement, and the optical Doppler effect. Dynamic speckles generally contain information about the movement of the image sample or the movement of particles within the sample.

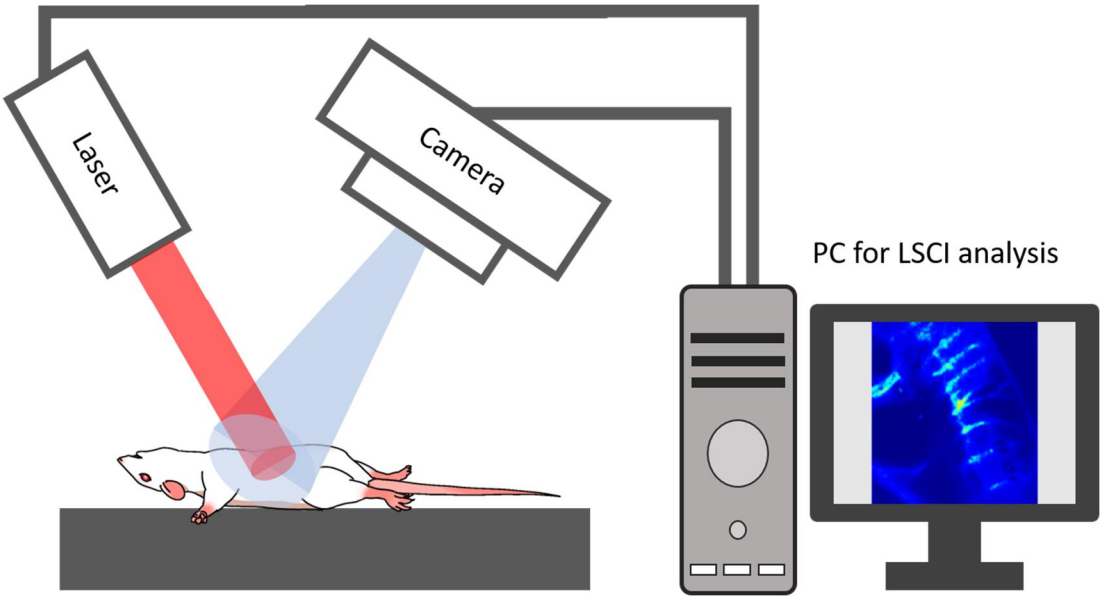

Figure 1. Schematic of general *in vivo* Laser Speckle Contrast Imaging setup

The speckle decorrelation time is a time scale that indicates how quickly the dynamic speckle pattern changes. To capture LSCI, the camera's exposure time must be similar to the speckle decorrelation time to accurately obtain information about the movement of particles within the tissue, such as red blood cells in blood vessels, from the blurring of the acquired speckle pattern. The speckle contrast K is calculated using the following formula through changes in the speckle pattern images:

$$K = \frac{\sigma}{\langle I \rangle} \quad \text{Eq. (1)}$$

where σ is the standard deviation of the intensity I and the mean intensity $\langle I \rangle$ from a window in space or time.

When moving scattering particles, such as red blood cells, exist within the imaging area, the speckle pattern changes, and the speckles become blurred. As a result, the speckle contrast K decreases, and the value of speckle contrast K extracts information about particle motion. Ideally, speckle contrast values are distributed between 0 and 1, with 1 indicating no movement.

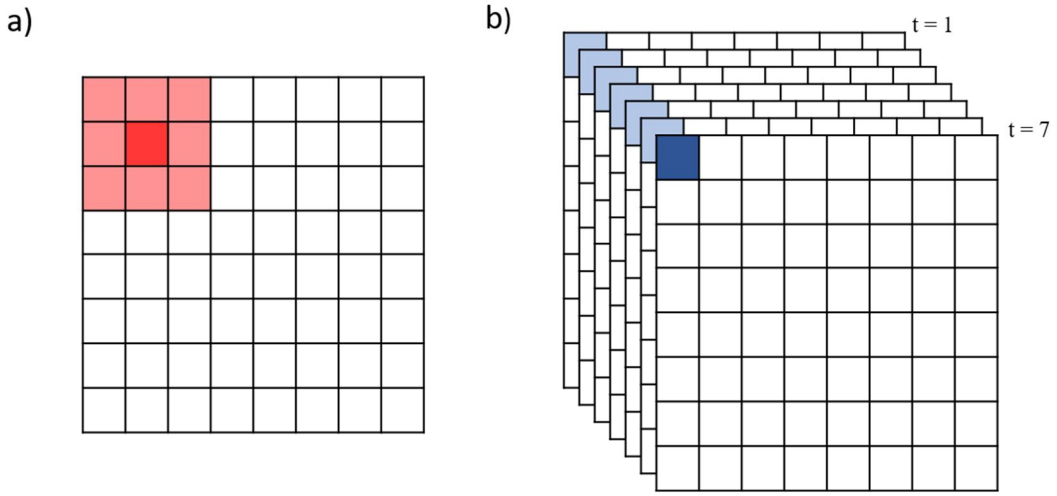

Figure 2. The pixel window for calculating speckle contrast K

a) a spatial pixel window (3x3 pixel), b) a temporal pixel window (7 frames)

Diffuse Reflectance Imaging (DRI)

In 2003, Andrew K. Dunn and colleagues were able to obtain images of cerebral hemoglobin oxygenation and total concentration using a multi-wavelength light source. [40] Since then, this imaging technique has been referred to as Diffuse Reflectance Imaging (DRI) or Intrinsic Signal Optical Imaging (ISOI) and has been predominantly studied for obtaining brain activation images in small animals, particularly in the field of neuroscience.[41, 42] DRI, similar to fMRI, enables the observation of changes in oxygenated and deoxygenated hemoglobin concentration to obtain brain activation information.[42] However, compared to MRI equipment, DRI can be configured with relatively simple light sources and cameras to obtain images, making it actively utilized in many neuroscience research areas.

DRI fundamentally relies on the distinct absorption spectra of oxyhemoglobin and deoxyhemoglobin. Hemoglobin in the blood is the most important light absorber in biological tissue in the visible and near-infrared wavelength bands. Moreover, oxyhemoglobin (HbO2) and deoxyhemoglobin (HbR) have different absorption spectra, allowing images obtained using different wavelengths of light to be primarily sensitive to the concentration changes of either HbO2 or HbR as shown in Figure 3 a). [43-47] Additionally, the change in total hemoglobin concentration can be calculated as the sum of the changes in HbO2 and HbR. To accurately calculate the actual changes in the concentrations of HbO2, HbR, and HbT, it is necessary to acquire tissue images at a minimum of two different wavelengths. This can be achieved by using multiple light sources with different wavelengths or by configuring a filter wheel that supports multiple wavelength bands in front of a white light source and synchronizing it with the camera to obtain images.

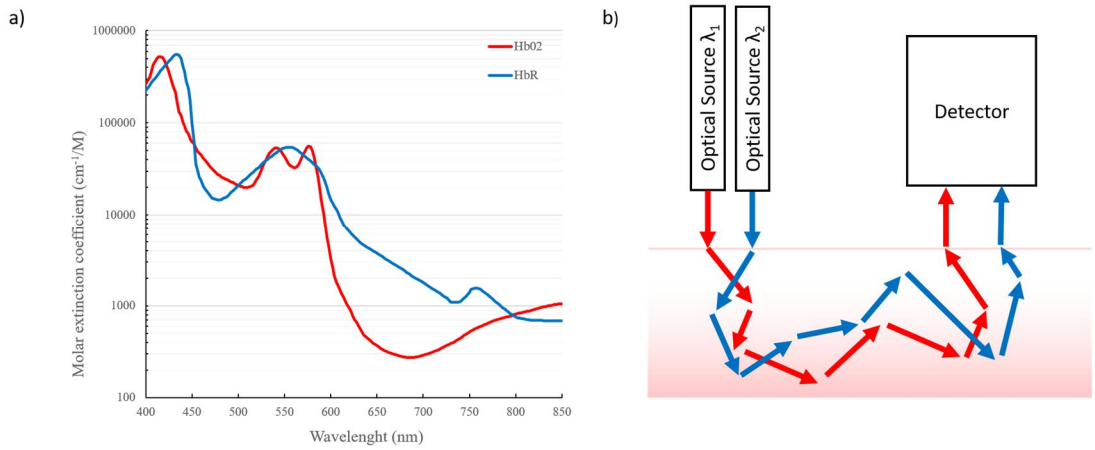

Figure 3. The hemoglobin absorption spectra and tissue light propagation scheme

a) oxy and deoxyhemoglobin absorption spectra at visible light wavelength band, b) Light propagation scheme at biological tissue with various scattering

To calculate the hemoglobin concentration in multi-wavelength images, it is necessary to consider the scattering effects of biological tissues and utilize known spectral data of HbO2 and HbR. This approach is based on the modified Beer-Lambert law and is defined as follows.

$$\frac{I}{I_0} = \exp(-\mu_a \mathrm{DPFx} + G)$$

where I is the measured light intensity, I_0 is the incident light intensity, DPFx is the mean pathlength of light traveled in biological tissue, G is the geometry-dependent factor, and μ_a is the absorption coefficient of the biological tissue. Furthermore, according to Beer's law, μ_a is the sum of the absorption coefficients of the n chromophores present in the biological tissue, and is defined as follows.

$$\mu_a = \sum_n \xi_n c_n$$

where ξ_n is the absorption coefficient of a specific chromophore at a particular wavelength, and c_n is the concentration of that chromophore.

I_0 is difficult to accurately determine in actual measurement environments, and G is also challenging to quantify. Therefore, typically, the changes in measured signals relative to an initial time point $t = 0$ are utilized. Under such conditions, the modified Beer-Lambert law can be redefined as follows.

$$\ln[\frac{I(t)}{I(t_0)}] = -[\mu_a(t) - \mu_a(t_0)]\mathrm{DPFx}$$

If images are acquired at two wavelengths λ_1 and λ_2, the changes in oxyhemoglobin concentration $\Delta[\mathrm{HbO}_2(t)]$ and deoxyhemoglobin concentration $\Delta[\mathrm{HbR}(t)]$ at time point t can be represented as follows.

$$\begin{bmatrix}\Delta[\mathrm{HbO}_2(t)]\\ \Delta[\mathrm{HbR}(t)]\end{bmatrix} = \begin{bmatrix}{\xi_{\mathrm{HbO}_2}}^{\lambda_1} & {\xi_{\mathrm{HbR}}}^{\lambda_1}\\ {\xi_{\mathrm{HbO}_2}}^{\lambda_2} & {\xi_{\mathrm{HbR}}}^{\lambda_2}\end{bmatrix}^{-1}\begin{bmatrix}\dfrac{\ln(I_{\lambda_1}(t_0)/I_{\lambda_1}(t))}{\mathrm{DPFx}_{\lambda_1}}\\ \dfrac{\ln(I_{\lambda_2}(t_0)/I_{\lambda_2}(t))}{\mathrm{DPFx}_{\lambda_2}}\end{bmatrix}$$

Since it is challenging to estimate the differential path-length factor values for each wavelength $\mathrm{DPFx}_{\lambda_1}$ and $\mathrm{DPFx}_{\lambda_2}$, Monte Carlo simulation models of light propagation paths are typically employed.

Additionally, the change in total hemoglobin concentration $\Delta[\mathrm{HbT}]$ can be calculated as follows.

$$\Delta[\mathrm{HbT}] = \Delta[\mathrm{HbO}_2] + \Delta[\mathrm{HbR}]$$

Based on these calculations, an imaging system combined with multi-wavelength light sources can derive and visualize the time-dependent changes in the concentration of oxygenated hemoglobin, deoxygenated hemoglobin, and total hemoglobin in biological tissues. Such imaging results are primarily used in research on visualizing brain activation regions through neurovascular coupling mechanisms,[48, 49] as well as in the quantification of breast cancer diagnosis and other ongoing studies.[50]

The smartphone-based endoscope system for high-speed vocal cord imaging

Introduction

High-speed digital imaging (HSDI), particularly high-speed endoscopic imaging, has recently become a routine diagnostic tool for vocal fold disorders.[51-60] However, the size and cost of high-speed digital endoscopic imaging devices often limit their accessibility for patients in underdeveloped countries or regions with insufficient medical infrastructure. Modern smartphones possess the necessary capabilities to process complex calculations required for high-resolution images and videos at high frame rates. There have been recent efforts to integrate medical endoscopes with smartphones to increase their availability in underdeveloped countries. The development of a smartphone adapter for endoscopes aims to reduce the cost of these devices and demonstrate the feasibility of high-speed vocal fold imaging using the advanced capabilities of high-performance smartphone cameras.

Method

Development of a smartphone-adapted endoscope

The development of a smartphone adapter for clinical endoscopy (Figure 4) was achieved by utilizing a standard 70° rigid endoscope (Karl Storz Co.). The adapter comprises a commercial smartphone holding parts, lenses, a lens tube, and mounts for the lens tube and endoscope connection. The adaptor was designed using 3D modeling software (Solid Works) and 3d printed by using an SLM 3D printer (Objet260, Stratasys Ltd.). A lens system was employed to magnify the endoscope probe eyepiece image, situated between the endoscope eyepiece and the smartphone camera, and held by 3D-printed components. To enhance cost-effectiveness, a combination of two simple bi-convex lenses was utilized for endoscopic image magnification instead of expensive achromatic lenses. With focal lengths of 50 mm and 15 mm, the optical setup facilitated the acquisition of approximately 1.5 × magnified images. Illumination was coupled through the endoscope's illumination port.

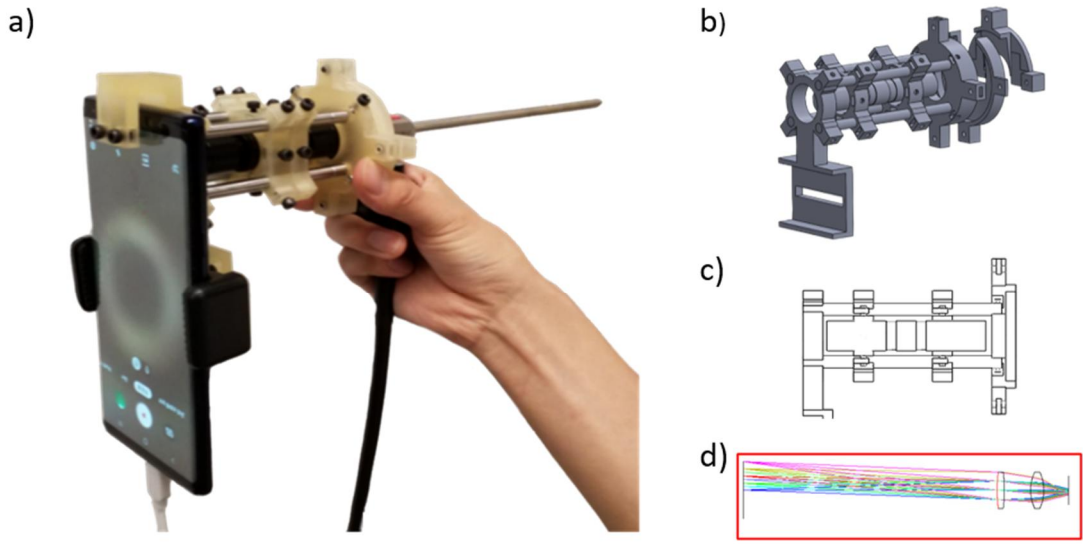

Figure 4. Development of a smartphone-adapted endoscope

a) a real operating image of the smartphone-adapted endoscope, b) the 3d model image of a smartphone endoscope adaptor, c) the cross-section image of the smartphone endoscope adaptor optical components part, d) an optical simulation image of the smartphone endoscope adaptor lens magnification system

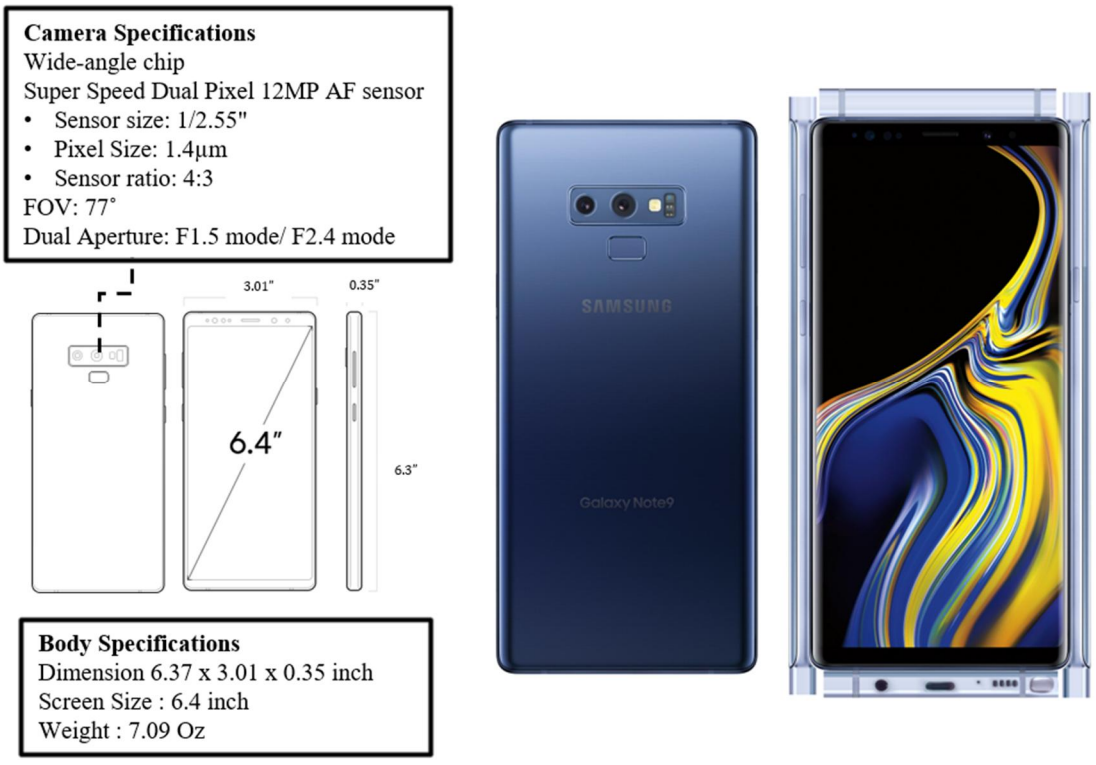

Figure 5. The image and specifications of the smartphone model (Galaxy Note 9, Samsung) used in developed smartphone-based endoscope device

A specific smartphone model (Galaxy Note 9, Samsung) was employed to capture high-frame-rate endoscopic images. According to the manufacturer's catalog specification, this particular smartphone model can acquire high-speed images at 960 fps for a maximum duration of 0.4 sec, with a resolution of 1280 × 720 pixels. The smartphone's complementary metal-oxide-semiconductor (CMOS) sensor is specified at 12.0-megapixels (MP), 1/2.55 inches (1.4 μm pixel size), and is equipped with an f/1.5-2.4 optical lens.

Image processing and data analysis

The high-speed vocal fold vibration images obtained were processed using the seeded region growing algorithm to ascertain the amplitude of the vibrations on either side of the glottis. Custom image analysis software was developed in MATLAB to compute diagnostic parameters such as vocal fold vibration frequencies, glottal edge phase shifts, and total glottal area volume variations.

Clinical trial

The developed smartphone-based imaging system was employed to obtain high-speed videos of the vocal folds of four human subjects, including one healthy individual and three patients with diagnosed vocal pathologies. A board-certified otolaryngologist at Asan Medical Center, with 15 years of experience, adhered to standard videokymography protocols to record high-speed diagnostic videos within a clinical setting.[52, 54] The human clinical study received approval from the Institutional Review Board of Asan Medical Center, Seoul (IRB #2020-0798), in compliance with the Korean Bioethics and Safety Act and the Korean Medical Device Act.

Before imaging human subjects, the smartphone-based high-speed imaging system was adapted to the clinical endoscope by adjusting the fine focus and securing the endoscope in position. After verifying the clarity and focus of the obtained images, the clinician conducted a routine vocal fold evaluation using the endoscope-smartphone device. Upon completion of the diagnostic routine, the endoscope probe was cleaned with a disinfectant to prevent cross-contamination between subjects. The entire procedure took under a minute, minimizing any unnecessary burden on the volunteers.

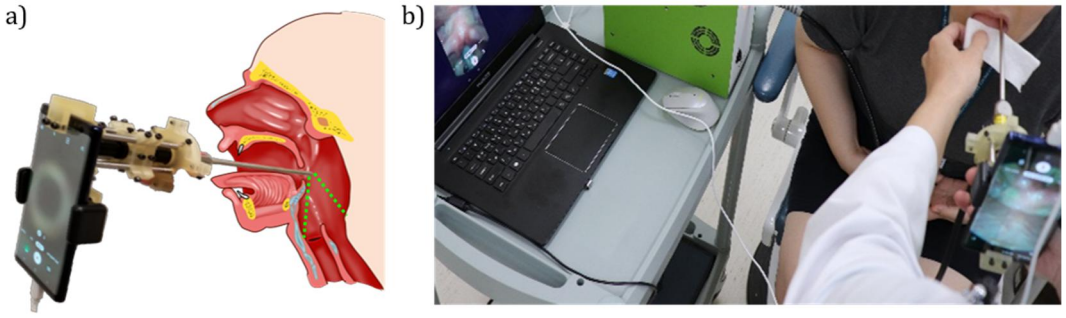

Figure 6. Clinical trials

a) schematic of clinical diagnosis of vocal fold imaging by using a developed smartphone-based endoscope device, b) image of the clinical diagnostic procedure using a developed smartphone-based endoscope device

Result

The HSDI vocal fold vibration videos, obtained using smartphone-based endoscopy, were taken through a clinical diagnosis process as shown in Figures 7 and 8. As illustrated in Figure 7, the 940 fps HSDI video from clinical experiments was segmented into the vocal fold area and glottal area for image processing, enabling quantitative analysis. This allowed us to acquire vocal fold parameters with the greatest contribution to clinical diagnosis. Quantitative image analysis of the HSDI vocal fold vibration data yielded the base vibration frequency of the vocal folds, the difference between the left and right glottal areas, and the total glottal area parameters.

As shown in Figure 7, HSDI vocal fold vibration video data from clinical diagnosis experiments were obtained from healthy subjects and patients with left vocal fold paralysis, chronic laryngitis, and right vocal cord polyps. The original RGB color image data were converted to grayscale, and the brightness and contrast were adjusted for glottal area segmentation using MATLAB. The seeded region growing method was used to segment only the glottal area from the image-processed data. The segmented glottal areas were divided into left and right areas by drawing the anatomical midline of the vocal fold under the consultation of a clinician.

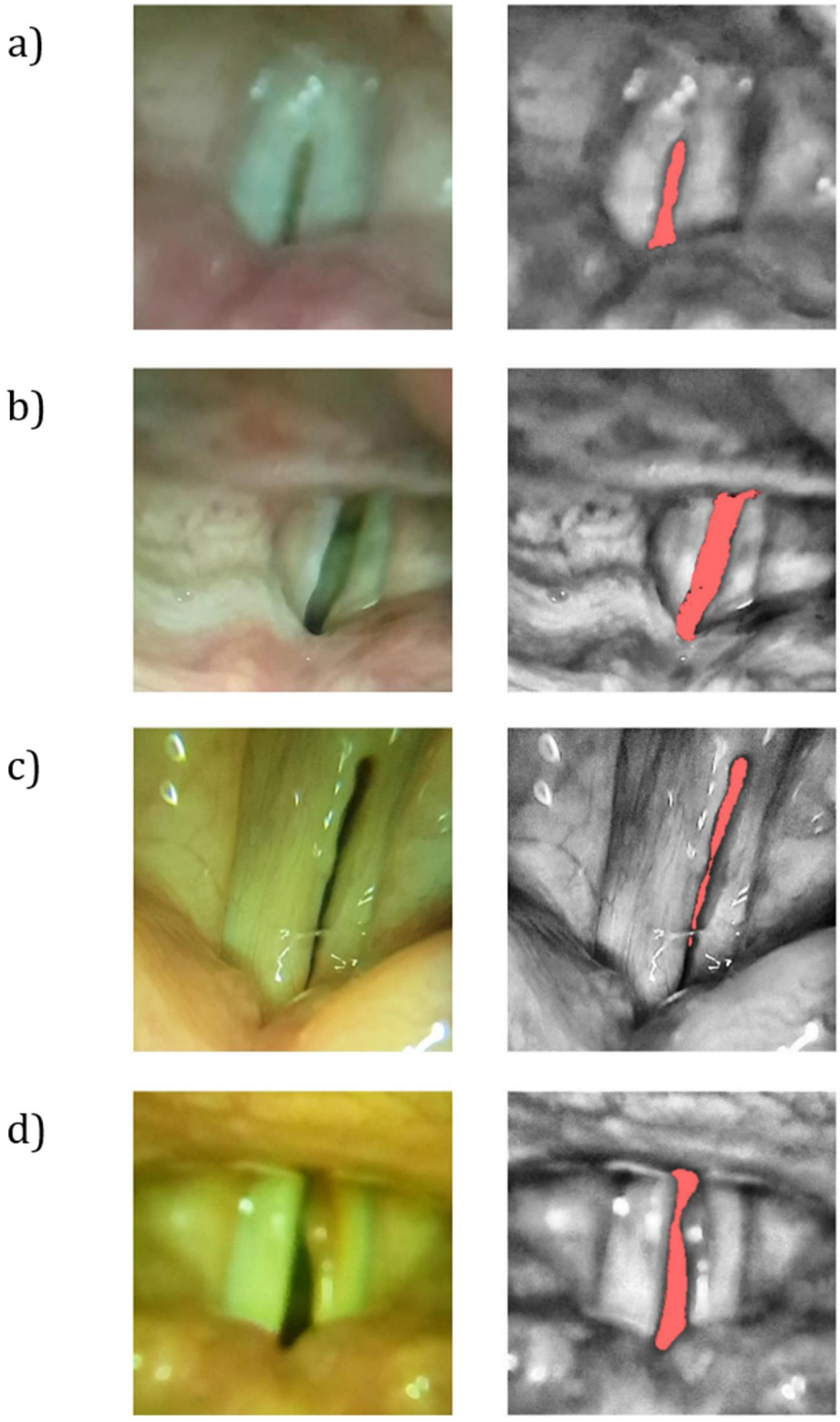

Figure 7. High-speed digital images of the vocal cord glottis and segmentation

Left: raw RGB vocal fold HSDI, Right: image processing result with red color glottis segmented area. a) Images of healthy volunteer, b) Images of left vocal cord paralysis patient, c) Images of chronic laryngitis patient, d) Images of right vocal cord polyp patient

The segmented glottal areas were quantitatively analyzed to determine any differences between the data of the healthy subject and those of patients. All data used in Figure 8 were normalized and displayed using the Fourier transform to remove motion error and calculate the base frequency of the vocal fold. As a result of calculating the change in the glottal area over time in a quantified manner, the fundamental frequency of a healthy 24-year-old female subject was 224 Hz. This confirmed that the calculated base frequency of the healthy subject was similar to the average base frequency of adult females of the same age group, around 217 Hz[61]. Figure 8 b) shows the normalized total and lateral (left and right) glottal area changes in the vocal cords of a patient suffering from left vocal fold paralysis. The data from this patient with left vocal fold paralysis showed that the amplitude of the left vocal fold vibrations was significantly lower than that of the right vocal fold due to reduced mobility caused by the paralysis. Figure 8 c) shows the normalized total and lateral glottal area changes in a patient with chronic laryngitis. Although the maximum amplitudes are similar for both the right and left vocal folds compared to the healthy subject, the minimum amplitude of each cycle is larger than that of the healthy subject. The minimum amplitude value of each cycle in the healthy subject is close to 0. This is because the vocal fold closes completely, and the glottal area disappears when voice is generated in a healthy subject. However, in patients with chronic laryngitis, the glottal area does not disappear completely and remains, as the vocal fold does not close entirely when generating voice. Figure 8 d) shows the normalized total and lateral glottal areas of the vocal cords in a patient with a polyp on the right vocal fold. In this case, the right vocal fold's mobility is restricted by the polyp, resulting in a smaller vibration amplitude of the right glottal area compared to the left glottal area. Similarly to chronic laryngitis, the patient with a right vocal fold polyp had much larger minimum areas than the healthy subject, indicating that the vocal folds do not close completely due to the polyp, leaving some glottal area remaining.

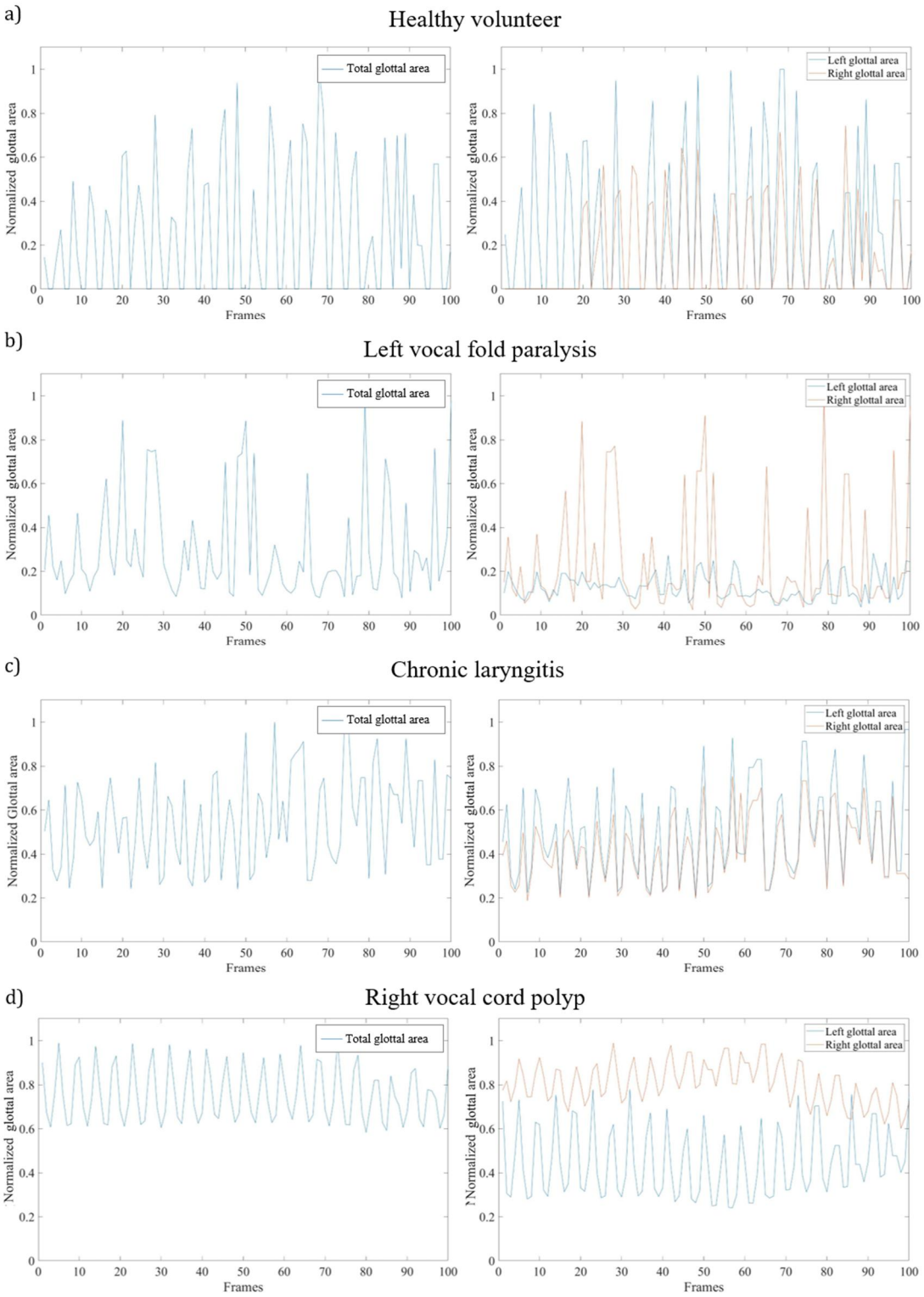

Figure 8. Plots of the quantified information

Left: Total glottal area, Right: Comparison of the left and right glottal area from glottal segmentation images of vocal cord HSDI a) plots of healthy volunteer, b) plots of left vocal fold paralysis, c) plots of chronic laryngitis, d) plots of right vocal cord polyp

Conclusion

This study aimed to develop a cost-effective and accessible smartphone-based endoscopy device to diagnose vocal cord diseases, targeting clinical diagnosis in otolaryngology. The device, composed of a conventional endoscope, a personal smartphone, a 3D-printed adapter, and low-cost optical components, demonstrated its potential by capturing diagnostic images at 940 fps. Analyzing these images enabled the calculation of diagnostic reference values, like the entire glottal area variation and left-right glottal area variations. Comparative analyses of healthy individuals and patients revealed discernible clinical features, suggesting the device's diagnostic potential. While the smartphone-based endoscope has a lower frame rate and other limitations compared to commercial High-Speed Digital Imaging (HSDI) systems, it is significantly cheaper, lighter, and has a higher video resolution.[62] Despite current limitations, the use of AI and future technological improvements could enhance the capabilities of this device,[63] potentially extending its application beyond vocal cord diagnosis to other areas as a Point-of-Care Testing (POCT) diagnostic device.

The smartphone-based flexible endoscope device uses laser speckle contrast imaging for point-of-care blood flow monitoring

Introduction

Laser speckle contrast imaging (LSCI) is universally recognized as a potent tool for the quantification of tissue blood flow due to its straightforward configuration, user-friendliness, and the intuitive nature of its results. Owing to substantial enhancements in the realm of smartphone and camera technologies, recent endeavors have focused on the creation of an LSCI application that can be utilized on smartphones. [31, 32, 64-66]. This application could function as a POCT device, providing an on-site examination of vascular anomalies. The development and validation of an innovative smartphone-oriented portable LSCI endoscope device now allow for *in vivo* endoscopic POCT assessments for the diagnosis of vascular disorders.

Method

Implementation of smartphone-based portable LSCI endoscope device

A cost-effective, smartphone-based portable LSCI endoscope has been engineered. The three-dimensional schematic of the system is illustrated in Figure 9 a), incorporating two principal components: a smartphone and an endoscope encapsulated within a 3D printed holder reminiscent of a handgun. The internal arrangement of the endoscope is elucidated in Figure 9. d), comprises a light source module, a fiberscope, and a lens unit. Within the light source module, a white LED (600 nm at a central peak in the spectrum, 2 W) was utilized for bright-field endoscopy, while a green laser diode (LD) (532 nm, 50 mW) functioned as a coherent light source for LSCI. Both were powered by battery-operated LED and LD drivers, managed by an Arduino microcontroller board integrated into the system. The lens unit was constituted of two achromatic lenses (L1 and L2) and an infinity-corrected 10 × objective (OBJ). L1 (f =

50 mm) and L2 (f = 3.1 mm) served as relay optics to transmit light from the OBJ to the focusing lens on the smartphone camera. A slender fiberscope (Myriad Fiber Imaging Inc.) with a flexible single-mode optical fiber bundle (FIGH-30-650S, 30,000 ± 3,000 pixels, Fujikura) (refer to the inset of Figure 9. b)) was employed as an endoscopic probe. The probe was situated between the light source module and the relay-lens unit. A pair of orthogonal linear polarizers (P1, P2) was placed before the LD and smartphone camera to mitigate strong specular reflection on the sample surface. This allowed the output beam from the light source to illuminate the interior of the body cavity through the fiberscope. Light scattered from within was captured by the fiberscope and transmitted to the relay-lens unit. A commercially available Android smartphone (Google Pixel 4a, 128 GB, 1080 × 2340 pixels, 143 g, 2020) was affixed to the endoscope using vertical and horizontal translation knobs to align the rear camera with the relay-lens unit. Endoscopy images (1024 × 720 pixels) were captured using the smartphone camera at an imaging speed of 120 FPS with 10 × optical magnification. Real-time imaging was displayed on custom-developed smartphone software or archived as a video (WebM file) on the smartphone for subsequent processing. Figure 9. c) presents the realized system prototype product (70 mm (width) × 150 mm (height) × 250 mm (length), under 1.2 kg). The total manufacturing cost of the device, excluding the fiberscope, was $1850.

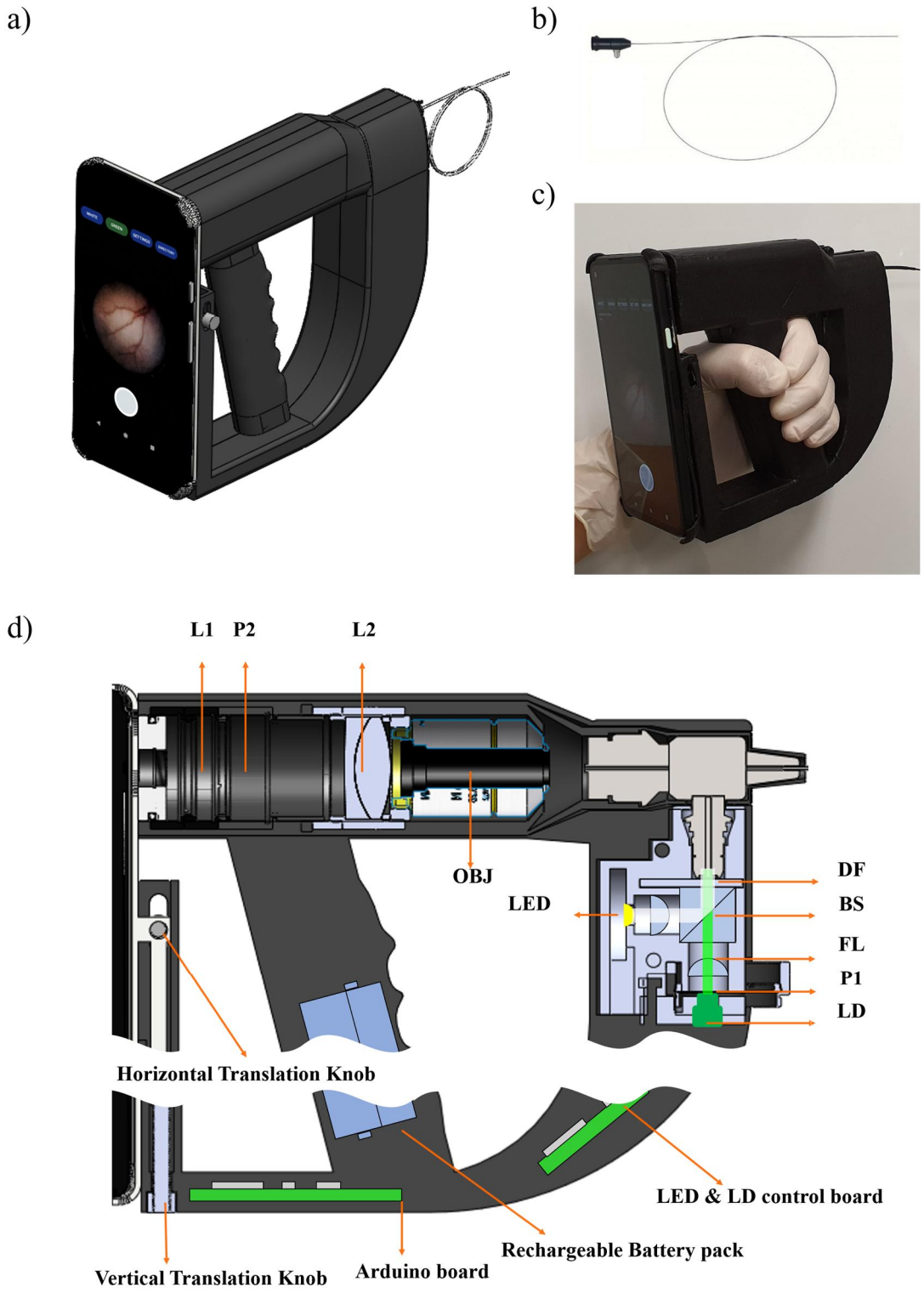

Figure 9. Smartphone-based LSCI endoscope system device.

a) 3D model design of a smartphone-based LSCI endoscope, b) image of adopted flexible optical fiber scope, c) a photo of manufactured smartphone-based LSCI endoscope device, d) internal parts configuration scheme of a smartphone-based LSCI endoscope

Our system offers two imaging modes for endoscopy and LSCI, facilitated by a custom-developed smartphone application. In endoscopy mode, the white LED is activated for bright-field examination of organ tissue. In LSCI mode, the light is rapidly switched to the green LD for coherent light illumination. In the LSCI mode, laser speckle patterns engendered by LD illumination on the tissue were captured as raw speckle images using the smartphone camera. The speckle image contains motion information of moving scatters, such as red blood cells (RBCs), leading to temporal alterations in speckle signals. To quantify the degree of speckle fluctuation, the speckle contrast K is typically defined as the ratio of the standard deviation of the light intensity over a region to the mean value between 0 and 1, which is proportional to the blood flow. In this study, we adopted the spatiotemporal laser speckle contrast analysis (STLASCA) methodology. [67] This approach aids in reducing image noise while preserving acceptable spatiotemporal resolution. To implement the STLASCA algorithm, 15 captured raw speckle images (1024 × 720 × 15 pixels) were converted to grayscale. A datacube (7 × 7 × 15 pixels) was subsequently obtained by overlaying a 7 × 7 pixel kernel on the grayscale image stack. The mean and standard deviation of the intensity of all pixels for each data cube were computed. Their ratio generated speckle contrast K. Upon the completion of kernel sliding, the output K value formed a speckle contrast image displayed on the smartphone screen.

Development of a user interface smartphone app for real-time endoscopy and LSCI

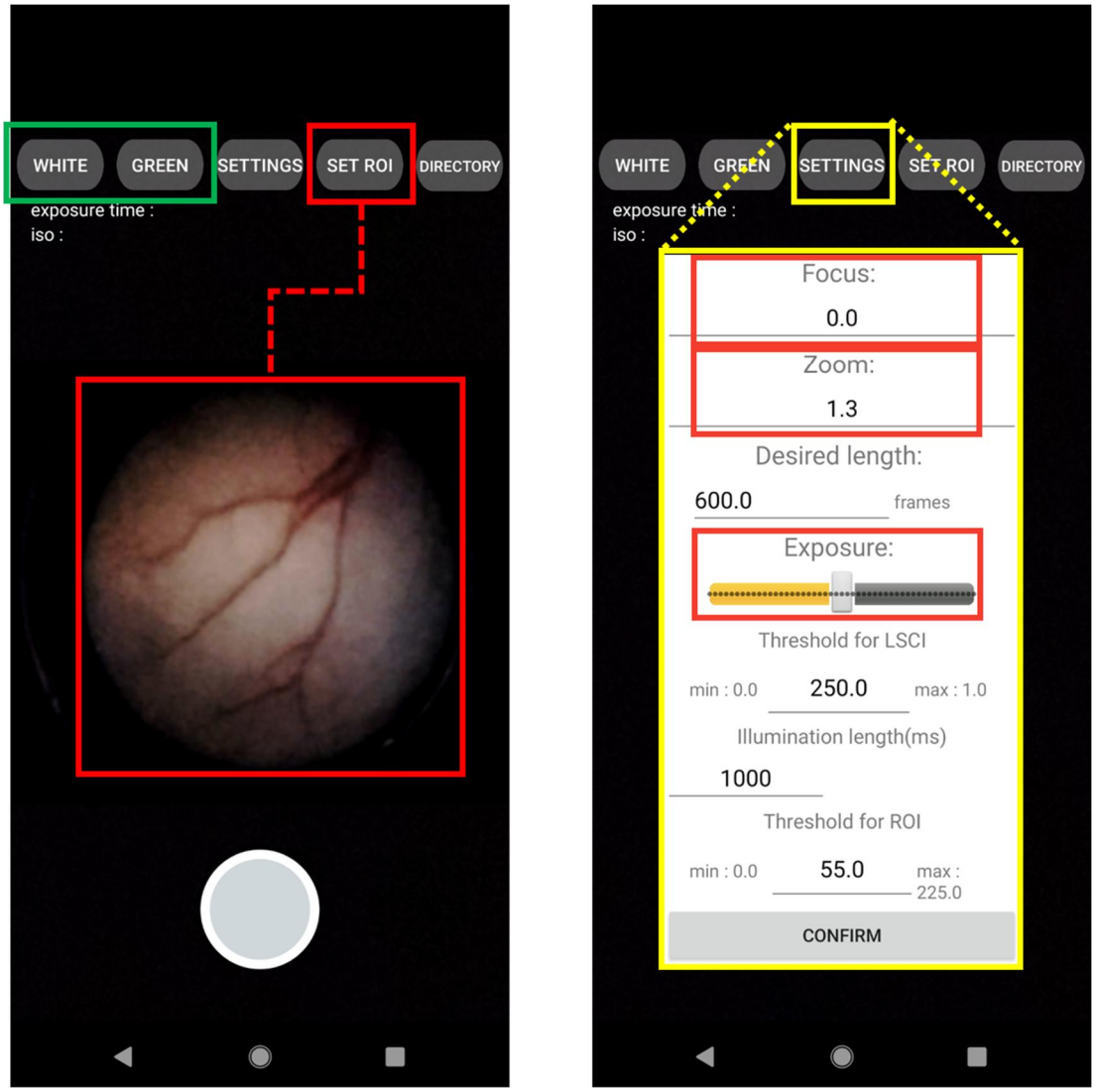

Figure 10. UI image of smartphone-based LSCI endoscope system's Android application.

An Android-based smartphone software with a straightforward and intuitive user interface (UI) was developed, enabling users to operate endoscopy and LSCI efficiently. The software was developed using Android Studio, the official Google Android development tool, employing Java and Kotlin languages. OpenCV, an open-source image-processing library, was harnessed for software development. Figure 10. depicts the primary pages of the smartphone-specific software. The figure includes button-type icons for mobile application functions. The UI's white and green buttons activate light sources to illuminate the sample for endoscopy and LSCI, respectively. Their outputs are displayed at 120 FPS as white-light images and raw speckle images on the app screen. The "SETTINGS" button opens a control box where users can adjust display parameters such as focus, digital zoom, and display brightness (see right in Figure 10.). The larger round button at the bottom of the app screen initiates video recording. When recording commences, the app screen can display LSCI images (K maps) computed with the raw speckle images at video output levels of > 30 FPS. The "SET ROI" button selects a region of interest (ROI) in the LSCI display. As illustrated in the flow chart in Figure 11., paired Bluetooth devices facilitate wireless communication between the app and the endoscope electronics.

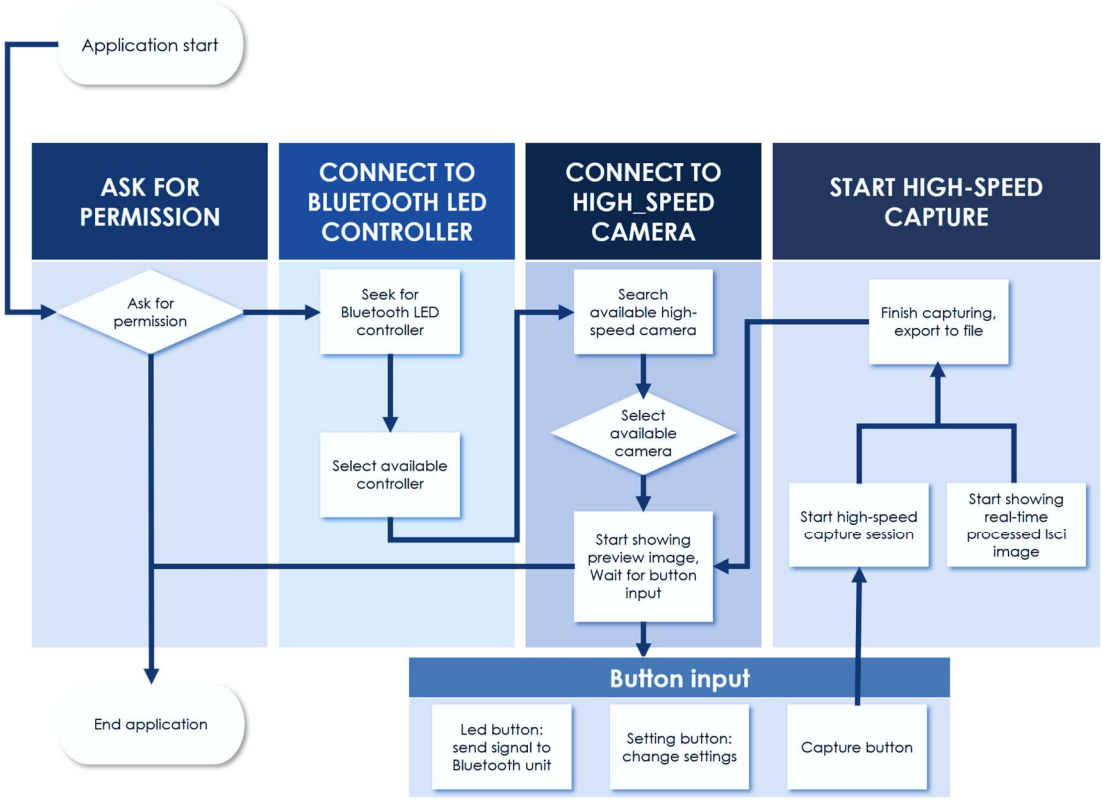

Figure 11. Flow chart of developed smartphone-based LSCI endoscope system' application

Tissue-mimicking phantom flow experiment

To evaluate the flow-imaging capability of the developed device, a scattering flow phantom was prepared. To emulate an optically turbid medium, akin to a tissue background, the phantom was composed of polydimethylsiloxane mixed with 0.15% (15 g/100 ml) TiO2. [68-70] A 2.5% microparticle solution was then injected into a transparent silicon tube of 1 mm diameter submerged in the phantom at steady flow rates ranging from 0.023 ml/min (0.5 mm/s flow speed) to 0.094 ml/min (2.0 mm/s flow speed) using a high-precision infusion syringe pump (Fusion 200, Chemyx Inc.). This effectively simulated the blood flow of a superficial vessel within stationary tissue. The device probe was positioned linearly 5 mm in front of the surface of the perfused phantom. The light from the probe tip illuminated the phantom for the LSCI measurement as shown in Figure 12.

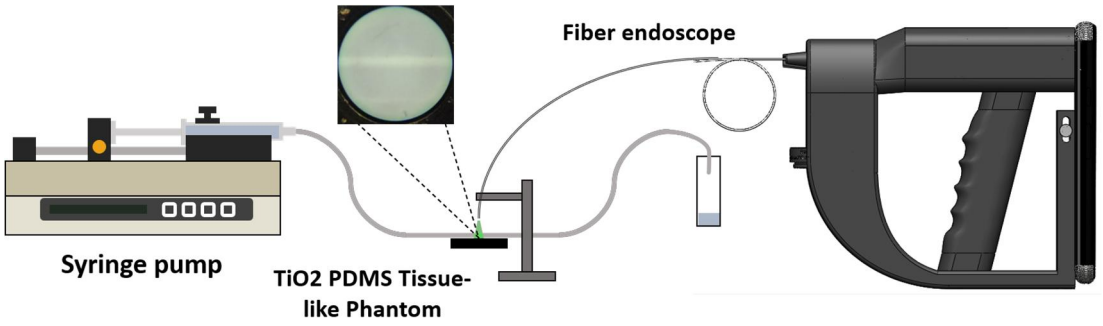

Figure 12. Experimental setup of the tissue-mimicking phantom flow experiment

In vivo small animal experiment

To assess the potential of the device for functional mobile endoscopy, we conducted *in vivo* small animal experiments using the device. The hollow organ urinary bladders of adult Sprague-Dawley rats were selected for cystoscopy due to the ease of access through the urethra with a thin fiber probe. To investigate vascular disorders in the bladder, bladder cancer rat models were established by administering N-butyl-N-(4-hydroxybutyl) nitrosamine (BBN) to the drinking water for seven months. This BBN-treated cancer model is the most frequently employed preclinical murine model of bladder carcinogenesis for accurately replicating human disease.[71, 72] It is responsible for high-grade invasive tumors of the urinary bladder. The normal rat (n=2) and the bladder cancer rat models (n=3) were anesthetized with an intravenous injection of 0.06% Zoletil and 0.04% Rompun per 100 g of body weight. The fully immobilized animal was placed on a temperature-controlled heating pad, and its bladder was emptied by applying gentle pressure to the bladder region. The emptied bladder was then rinsed five times with phosphate-buffered saline (PBS). Following the bladder wash, the flexible endoscope fiber tip of the device was gently inserted into the urethra and carefully directed toward the bladder site through the urinary tract. After navigating through the bladder lumen of a normal rat, the probe tip was situated at the bladder wall with vascularity. The tip was positioned at the observable tumor mass in the bladder cancer model for endoscopy and LSCI measurements. All experimental animal procedures were reviewed and approved by the Institutional Animal Care and Use Committee of the Asan Medical Center (Protocol number: 2020-12-111).

Result

Tissue-mimicking phantom flow experiment

Figure 13 shows the results of flow experiments on an LSCI (Laser Speckle Contrast Imaging) phantom mimicking the human tissue, developed for a smartphone-based endoscope device. The raw speckle images obtained with a green laser were analyzed using spatiotemporal methods to calculate the speckle contrast value, K. To investigate the correlation between K and flow rate, K values were transformed into Speckle Flow Index (SFI) values, defined as 1/(2TK^2), where T is the exposure time of the smartphone camera.[73] The exposure time value for the acquired images with the developed device was 8.33ms. SFI values are proportional to the flow rate, as shown in Figure 13 a), where lower flow rates result in smaller SFI values in the mapping image, and higher flow rates result in higher SFI values in the mapping image. The plot in Figure 13 b) shows the average SFI value of the same area representing the flow rate in the mapping image, calculated quantitatively, along with the actual flow rate. This confirms a direct proportionality between the actual flow rate and the SFI value.

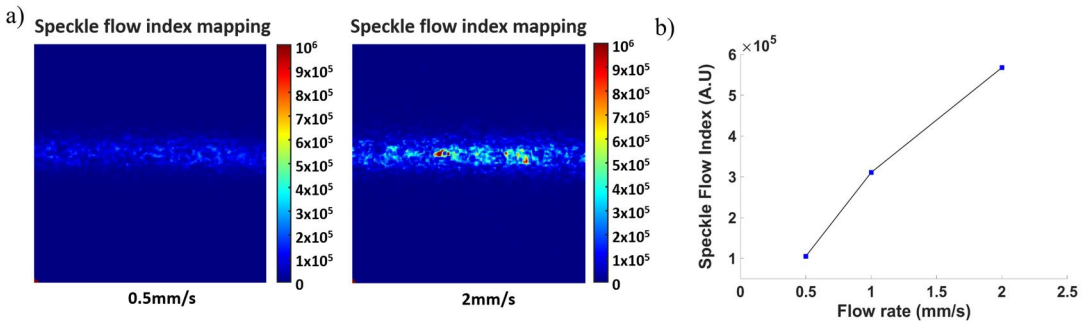

Figure 13. Tissue-mimicking phantom flow experiment result.

a) Speckle flow index (SFI) images of the tissue-mimicking phantom (Left: 0.5mm/s, Right: 2mm/s), b) plot of the SFI values at the different flow rate image data

In vivo small animal experiment

After confirming the successful acquisition of LSCI images using a phantom mimicking human tissue, experiments were conducted to obtain LSCI images of actual biological tissue., we acquired the LSCI endoscope blood flow imaging from a normal rat bladder (n=2) and BBN-induced cancerous rat bladders (n=3) *in vivo* as shown in Figure 14. a) and the acquired white light video and green laser raw speckle video results are shown in Figure 14. b) and c). Figure 14. b) shows the blood vessel images inside the bladders of two normal rats, while Figure 14. c) displays blood vessel and tumor images inside the bladders of two BBN-induced bladder cancer model rats. To convert the acquired image data from the normal rats and the BBN-induced bladder cancer model rats into LSCI images, the data was transformed into grayscale speckle images, and speckle contrast mapping image results were obtained. Figure 15. a) and 15. c) show the grayscale speckle images for the normal and BBN-induced bladder cancer rats, respectively, while Figure 15. b) and 15. d) depict the speckle contrast images for the normal and BBN-induced bladder cancer rats, respectively. As can be seen in Figure 15. b), the speckle contrast images allowed the clear observation and distinction of vascular structures. In the case of Figure 15. d), blood vessels within the bladder tumor, which were not properly visible in Figure 15. c), were distinctly identifiable. Through the LSCI images of the bladder tumor's blood vessels, it was confirmed that the bladder tumor is growing by utilizing the tumor vasculature connected to the surrounding bladder vessels.

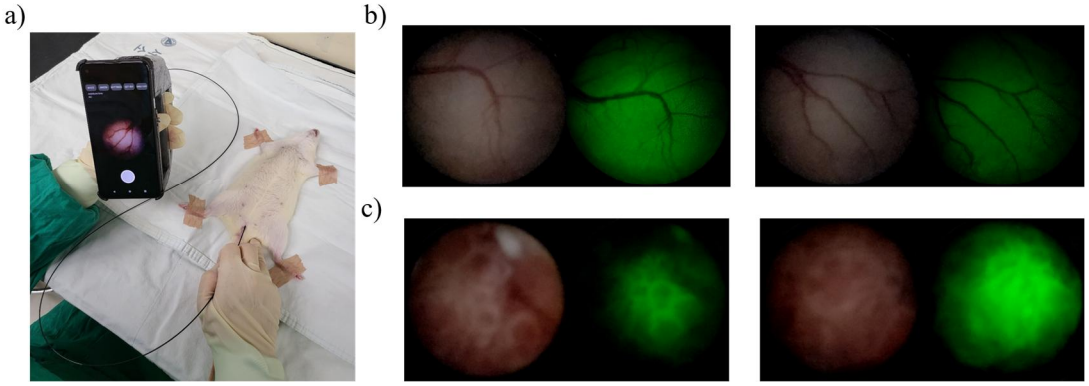

Figure 14. ***In vivo*** **rat bladder vascular imaging with smartphone-based LSCI endoscope device,**

a) rat bladder vascular images were acquired by a clinician using the developed device, b) white light image and green laser raw speckle image of the normal rat bladder blood vessel, c) white light image and green laser raw speckle image of the BBN-induced cancerous rat bladder blood vessel

a)

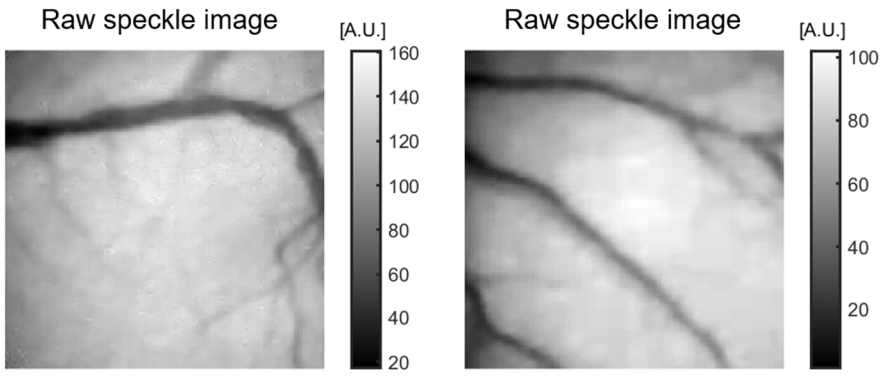
Raw speckle image
[A.U.]
160
140
120
100
80
60
40
20
Raw speckle image
[A.U.]
100
80
60
40
20

b)

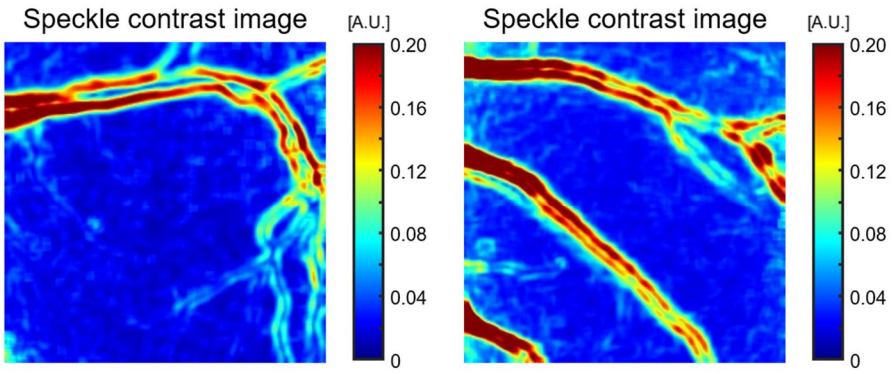
Speckle contrast image
[A.U.]
0.20
0.16
0.12
0.08
0.04
0
Speckle contrast image
[A.U.]
0.20
0.16
0.12
0.08
0.04
0

c)

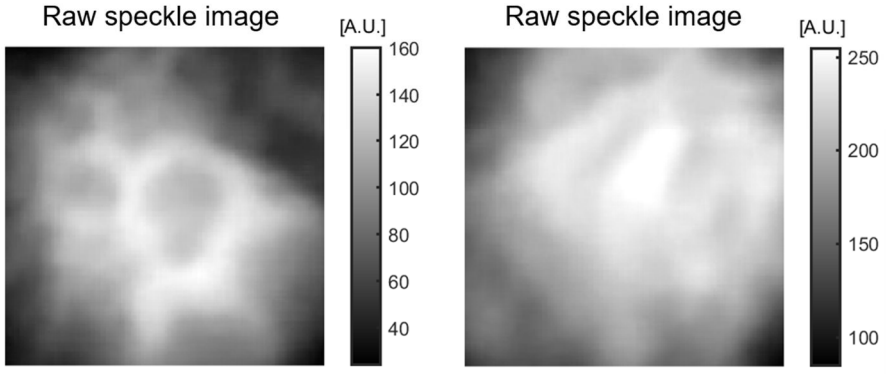
Raw speckle image
[A.U.]
160
140
120
100
80
60
40
Raw speckle image
[A.U.]
250
200
150
100

d)

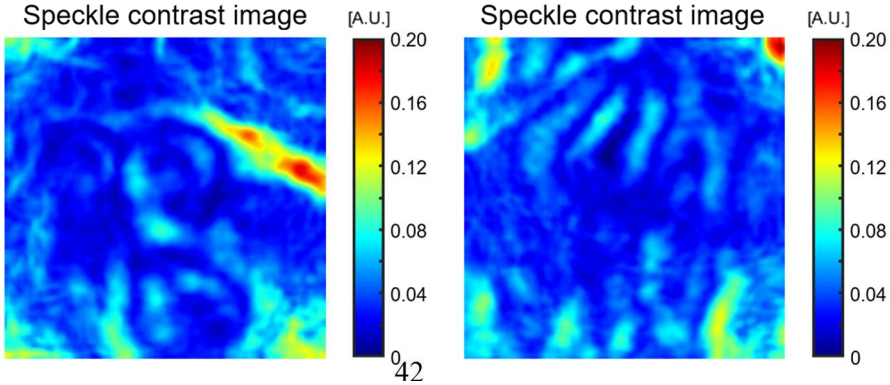
Speckle contrast image
[A.U.]
0.20
0.16
0.12
0.08
0.04
0
Speckle contrast image
[A.U.]
0.20
0.16
0.12
0.08
0.04
0

Figure 15. Image processed result of the rat bladder vascular image.

a) grayscale raw speckle image of the normal rat bladder vessel. b) speckle contrast mapping image of the normal rat bladder vessel, c) grayscale raw speckle image of the BBN-induced cancerous rat bladder vessel. b) speckle contrast mapping image of the BBN-induced cancerous rat bladder vessel,

Conclusion

In this study, we developed an endoscopic system integrated with smartphone cameras capable of capturing Laser Speckle Contrast Imaging (LSCI) images, using both conventional endoscopic images and LSCI images with a white LED and green laser. The increased performance of modern smartphones, allowing for 120fps video capture, even in low-cost models, made LSCI image acquisition feasible. While LSCI can offer more diverse biological imaging information [74-76], its clinical application has been limited due to the need for additional equipment. However, our smartphone-based LSCI endoscopy system, validated through phantom experiments and *in vivo* rat models, suggests potential future application as a clinical diagnostic tool for Point-of-Care Testing (POCT). Despite currently only capturing LSCI images with a single wavelength laser source, the system design and fabrication process indicate the possibility of incorporating additional laser light sources for a broader range of functional images.

The smartphone-based rigid endoscope system combining LSCI & hemodynamic response imaging

Introduction

The previously developed smartphone-based endoscope devices have demonstrated potential for clinical diagnostic utilization as Point-Of-Care (POCT) equipment and have improved the feasibility of using functional imaging techniques for POCT clinical applications. [77] Having previously confirmed an increase in POCT clinical diagnostic possibilities with the addition of Laser Speckle Contrast Imaging (LSCI) image analysis alone,[37, 76, 78-80] the subsequent aim was to explore options that allowed the acquisition of additional functional images without losing the advantages of using smartphone-based endoscope devices as POCT equipment. A previous research team identified a hyperspectral imaging analysis method, which was one of the functional image analysis techniques that could be combined with LSCI in preclinical and clinical settings.[81] For verifying appropriate vascular connections in clinical environments after surgery, it was deemed more effective to observe tissue damage and recovery levels caused by vascular connections utilizing hemodynamic response imaging obtained through hyperspectral imaging, in addition to LSCI-provided blood flow imaging.

To validate this approach, previous research simulated vascular severing and reconnection that may occur in surgical procedures by artificially blocking the blood flow in the rat's small intestine vessels using clamping, releasing the clamping after a certain period, and restoring blood flow. In this *in vivo* experiment, LSCI and hyperspectral images were simultaneously combined, providing blood flow and tissue oxygen saturation change images, which may increase the possibility of successful surgical outcomes as a supplementary tool. This research demonstrated the potential applicability of smartphone-based endoscope POCT equipment for clinical diagnosis when providing not only LSCI blood flow images but also tissue oxygen

saturation images.

Therefore, the goal of this study was to develop a smartphone-based endoscope device that could provide both LSCI blood flow images and tissue oxygen saturation images. The developed device was tested for its ability to acquire LSCI and hemodynamic imaging in phantom and biological tissue experiments. The aim was to validate the effectiveness of the smartphone-based endoscope POCT device as a diagnostic tool by detecting ischemic tissue damage and vascular abnormalities in internal organs.

Method

Development of a smartphone-based endoscopy using RGB laser for LSCI & hemodynamic response imaging

We have engineered a multi-modal, smartphone-integrated rigid endoscope device, as depicted in Figure 16. The device is ergonomically designed for handheld use, incorporating a rigid endoscope, and constructed with components printed via a 3D printer. A comprehensive 3D schematic of the system is exhibited in Figure 16. b), showcases two principal constituents: an adapter for a smartphone rigid endoscope furnished with optical components, in addition to electronics paired with a laser light source.

The inner structure of the system is demonstrated in Figure 16. a), elucidates the relative positioning of the integrated Red-Green-Blue (RGB) laser source module, the rigid endoscope, and the optical constituents. The RGB laser source module comprises a 638 nm 150 mW red laser diode, a 520 nm 70 mW green laser diode, a 488 nm 45 mW blue laser diode, and a laser diode module driver responsible for the operation of the lasers. The module is regulated by an embedded Arduino microcontroller board within the device, and energized by rechargeable

Li-ion batteries.

Between the optical source port of the rigid endoscope and the laser output port of the RGB laser module, two optical elements are employed to augment the imaging quality. An optical diffuser (OD) ensures uniform laser illumination, and an optical polarizer (P1) is deployed to eliminate specular reflection. Furthermore, the optical components - including lenses, diffusers, and polarizers - were procured from Thorlabs (NJ, USA).

The optical components situated between the rigid endoscope and the smartphone camera consist of two achromatic lenses (L1, L2) and an optical polarizer (P2). The union of L1 (f = 50 mm) and L2 (f = 3.1 mm) functions as relay optics to efficiently convey light from the camera connector image surface of the rigid endoscope to the focusing lens on the smartphone camera. To attenuate strong specular reflection on the sample surface, a pair of orthogonal linear polarizers (P1, P2) are strategically positioned in front of the RGB laser module and the smartphone camera, respectively. A commercially accessible laryngoscope (Hinode, China) is repurposed as the rigid endoscope in our system, featuring a 0°, 4 mm diameter, 175 mm length endoscope probe, a light port compatible with Wolf and Storz, and a camera connector.

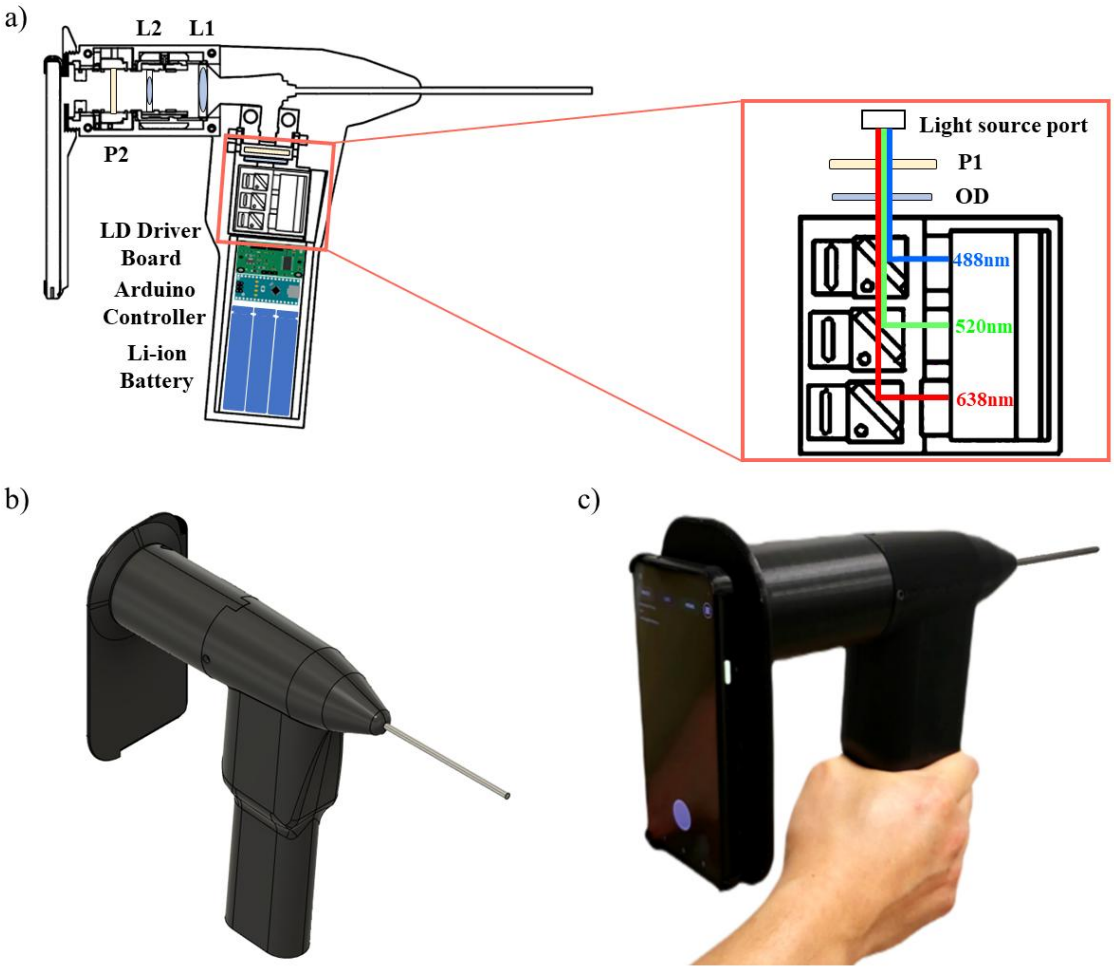

Figure 16. Development of smartphone-based multi-modal rigid endoscope system.

a) Internal structure scheme of the developed system, b) 3d model design of the developed system, c) photo of produced smartphone-based multi-modal rigid endoscope system

A commercially procurable Android smartphone (Pixel 4a, Google, CA, USA) is affixed to the endoscope using a 3D-printed smartphone adapter. The final endoscopic video acquires 120 frames per second at a resolution of 1024 pixels × 720 pixels for subsequent processing. Figure 16. c) portrays the implemented system as developed. The ultimate system measures 60 mm (width) × 180 mm (height) × 280 mm (length) and weighs less than 2 kg.

The devised multi-modal system is capable of acquiring three distinct imaging modes via a proprietary smartphone application (elucidated in the subsequent section). Essentially, the system can simultaneously illuminate three different wavelength lasers, allowing users to observe bright field endoscopy images in real-time.

By employing the Arduino control board, the system can exclusively illuminate the 638 nm red laser on the sample surface, and solely image data from this red 638 nm laser provides Laser Speckle Contrast Imaging (LSCI) information. Video data from the 638 nm laser speckle encompasses temporal speckle-noise pattern alterations instigated by flowing scatterers such as red blood cells (RBCs), which can be transformed into flow data. The degree of fluctuations of the speckles, typically denoted as the speckle contrast K, is defined as the ratio of the standard deviation of the light intensities over a region to the mean value. This ratio, which ranges between 0 and 1, is proportional to the blood flow. Among various strategies for calculating the speckle contrast K, our system employs a Temporal Laser Speckle Contrast Analysis (TLASCA) method, which facilitates a reduction in image noise while maintaining acceptable spatiotemporal resolution. To implement the TLASCA algorithm, the acquired 15 raw speckle images (1024 × 720 × 15 pixels) are converted into grayscale images. The mean and standard deviation of the intensities at all pixels in each image pixel position is computed, and their ratio generates the speckle contrast K. Consequently, upon completion of the

sequential image calculation, the output of K values comprises a speckle contrast image that represents flow velocity. Before LSCI and hemodynamic computations, raw images undergo post-processing in the Android application, which includes noise reduction and intensity normalization measures, such as moving averages.

Moreover, our system can analyze hemodynamic information by employing the concurrently captured RGB video. Numerous existing multi-channel wavelength hemodynamics monitoring systems utilize switching mechanisms for either the light source or the detection channel to ascertain light intensity information for each wavelength band. In contrast, our system determines hemodynamic information using continuous images without the necessity of switching light sources or filters. The developed system illuminates only the 488 nm laser and the 638 nm laser during the acquisition of hemodynamic video data.[82, 83] Considering the camera sensor sensitivity spectrum, we minimized inter-channel interference by selecting only the blue 488 nm channel and red 638 nm channel for hemodynamic changes computation. The modified Beer-Lambert law is typically employed for the calculation of these hemodynamic changes. We assumed that the relative concentration changes of oxy-hemoglobin (Δ) and deoxy-hemoglobin (Δ) dominate the light absorption of each component concentration change. Based on this assumption and the modified Beer-Lambert law, we can provide maps of relative hemodynamic changes.

Development of a smartphone app user interface for real-time endoscopy and LSCI

To facilitate the operation of the endoscopic device via a smartphone display, a bespoke smartphone application was conceived to augment the device. The procedural flow of the application is succinctly delineated in Figure 17. a) Following the verification of permissions for the camera, storage, and Bluetooth, a connection is established with the Bluetooth laser light source control module. Once an appropriate camera for high-speed capture is selected, a preview image is displayed, awaiting user command. Figure 17. b) depicts the user interface screen, designed for primary previewing, recording, and real-time image processing of Laser Speckle Contrast Imaging (LSCI) and hemodynamics.

The application was developed utilizing Android Studio (Google, CA, USA). The user interface was specifically architected to provide users with intuitive command over the device, with all control options and adjustment of settings conveniently available on the display. The upper segment of the interface houses direct controls for the laser light source and a settings button. The comprehensive settings menu is only revealed when the settings button is engaged, minimizing visual clutter for the user. Activation of the settings menu button alternates detailed settings for the laser light source, Bluetooth connection to the laser light source module, options for LSCI and hemodynamic image processing, and camera settings. For the laser light source, users can modify illumination duration, intensity, and color options. The Bluetooth connection button facilitates reconnection to the module. The Region of Interest (ROI) setting enables automatic adjustment for the region of interest. For LSCI and hemodynamic image processing, users can alter the image threshold and the processing method. Finally, the camera settings menu allows for adjustments of focus, zoom, record duration, and relative ISO value. On pressing the record button (located at the bottom), the recording of high-speed images initiates simultaneously, processing and displaying the processed image of either LSCI or

hemodynamics, as per the user's selection. The real-time computation of LSCI and hemodynamics is enabled by the implementation of the OpenCV library within the application.

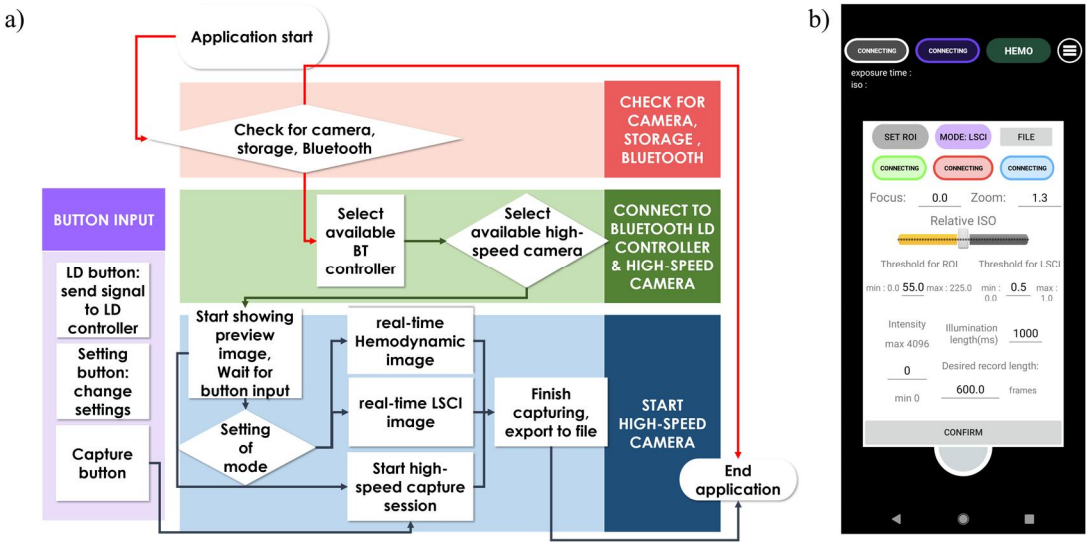

Figure 17. Development of smartphone-based multi-modal rigid endoscope system's smartphone app

a) a flowchart of the developed smartphone app, b) a UI screen of the developed smartphone app

Tissue-like flow phantom experiment

To corroborate the Laser Speckle Contrast Imaging (LSCI) capabilities of the engineered system, we constructed a scattering flow phantom, emulating tissue-like properties. The flow phantom was composed of polydimethylsiloxane (PDMS) amalgamated with 0.15% (15 g/100 ml) TiO2, to mimic an optically scattering milieu analogous to in-vivo tissue backdrop.[68-70] For the formation of the flow phantom mold, a metal tube with an outer diameter of 1 mm was employed, thereby creating a flow channel of 1 mm diameter within the flow phantom. A high-precision infusion syringe pump (Fusion 200, Chemyx Inc.) was utilized to modulate the flow rate of a 2.5% micro-particle solution, ranging from 0.023 ml/min (equating to a flow speed of 0.5 mm/s) to 0.094 ml/min (corresponding to a flow speed of 2.0 mm/s). This was done to simulate the blood flow of a superficial vessel within biological tissue, and the flow rates were validated using an inverted microscope. A system holder ensured the rigid endoscope probe's position was maintained at a distance of 5 mm from the surface of the flow phantom.

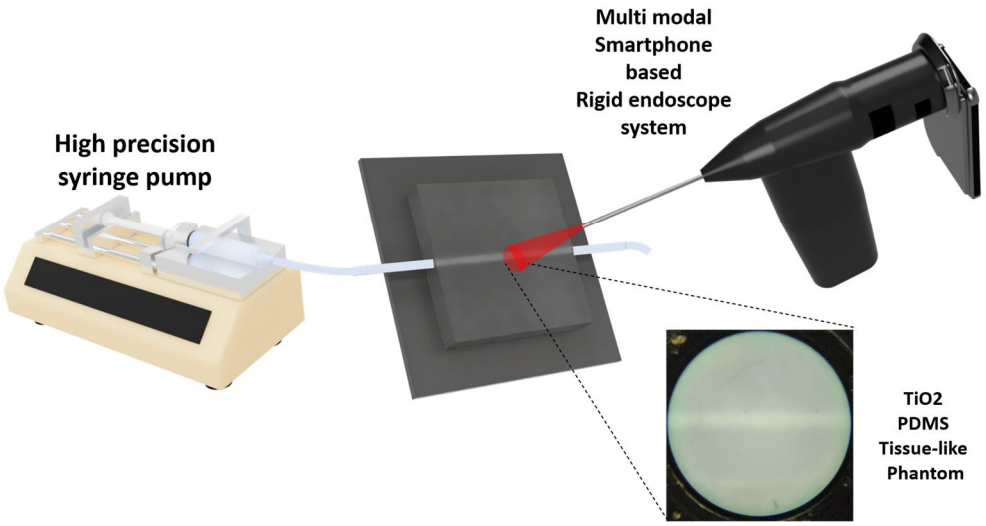

Figure 18. Experiment setup for LSCI capability using tissue-like flow phantom and multi-modal smartphone-based rigid endoscope system

In vivo rat ischemia experiment

To validate the operational efficacy of the devised multi-modal smartphone-based rigid endoscope system, we subjected it to *in vivo* rat ischemia experiments. Eight-week-old Sprague-Dawley rats (n=3) were anesthetized via intravenous administration of a compound of 0.12% Zoletil and 0.08% Rompun, proportionate to 200 g of body mass. The fully anesthetized specimen was positioned on a thermally-regulated heating pad. We executed a minimally invasive midline laparotomy and unveiled the small intestine for ischemia imaging. Both ends of the marginal artery in the imaging target area were constricted, and the main artery was clamped to simulate ischemic conditions, as delineated in the protocol for inducing intestinal ischemia-reperfusion injury in small animals.[84] All experimental procedures involving animals were scrutinized and authorized by the Institutional Animal Care and Use Committee (IACUC) of Asan Medical Center (Protocol number: 2020-12-111), in compliance with the Laboratory Animal Law of the Republic of Korea.

Result

Tissue-like flow phantom experiment

Upon the completion of the design and fabrication of the smartphone-integrated multimodal rigid endoscope device, we evaluated the Laser Speckle Contrast Imaging (LSCI) capacity of our system on a tissue-mimicking phantom, as portrayed in Figure 18. In the initial stage, we gathered bright field images under concurrent RGB laser illumination, facilitating the adjustment of focus and lighting intensity to correspond with the conditions of the tissue-mimicking flow phantom. The laser diode operation function in the custom-developed application was employed to illuminate the phantom with a 638 nm red laser for LSCI examination. Video data, with a resolution of 1024 × 720 pixels, was captured at 120 frames per second and subsequently transformed into Speckle Flow Index (SFI) maps, computed as 1/(2TK2), wherein T denotes the camera exposure time and K represents the speckle contrast, the ratio of speckle to mean intensity. In the video capture settings of our device, the exposure time (T) of the smartphone camera was 8.33 ms. As delineated in Figure 19 a) and b), the SFI images of the tissue-mimicking flow phantom at velocities of 0.2 mm/s and 2.0 mm/s demonstrate that superior flow rates correspond to augmented SFI values, while inferior flow rates correspond to diminished SFI values. This evidence posits that our newly developed system might be capable of imaging perfused structures within biological tissue.

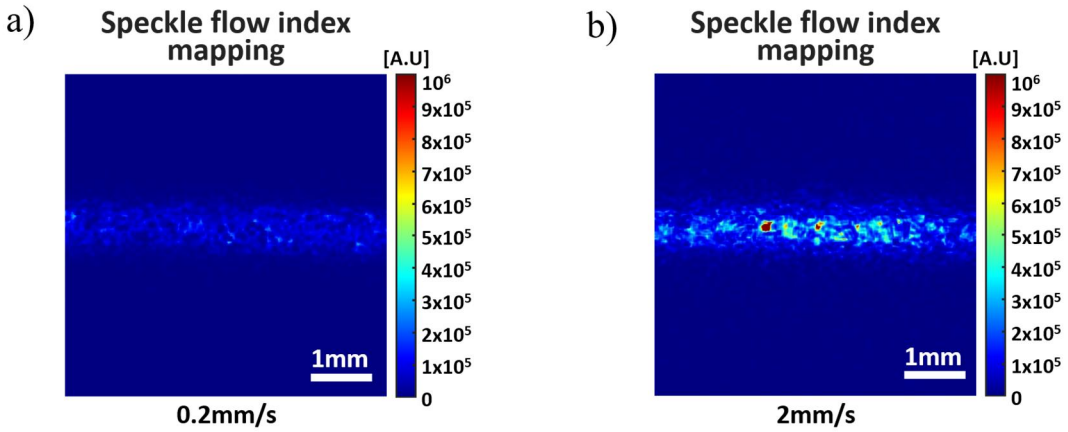

Figure 19. SFI mapping image of tissue-like flow phantom experiment result.

a) 0.2mm/s flow case, b) 2mm/s flow case

In vivo rat ischemia experiment

After verifying the basic light source control and imaging acquisition performance of the developed smartphone-based multimodal rigid endoscopic device using a tissue-like flow phantom, we aimed to acquire *in vivo* tissue images using small animals and verify whether the developed device can properly implement LSCI and tissue oxygen saturation change images. To do this, an *in vivo* rat ischemia mimic experiment was conducted by anesthetizing the rat, incising the abdomen, exposing the small intestine, and then artificially blocking and releasing the major arteries of the small intestine. Figure 20. a) shows the exposed small intestine of the anesthetized rat placed beneath the endoscopic tip of the developed smartphone-based endoscope. The white arrow is a stainless steel clamp fixed to block blood flow to the area of interest marked with a yellow box, and polypropylene sutures were used to tie the edge arteries at both ends of the ischemic area marked with a yellow box to block blood flow from outside the area of interest. In this experimental environment, the stainless steel clamp was fixed and released on the major artery of the area of interest to control the blood flow supplied to the small intestine's area of interest. Figure 20. b) and c) are 638nm laser raw speckle images for obtaining LSCI data in the area of interest under clamping and clamping released situations, respectively. The acquired 638nm laser raw speckle images were then calculated for speckle contrast and ultimately converted into mapping images representing the SFI value, which is proportional to blood flow. These are shown in Figure 21. a) and b) show the disappearance of blood flow in the area of interest below the edge vasculature sutures indicated by the red arrows due to clamping. Figures 21. c) and d) show the opposite, with blood flow reappearing as clamping is released. These results confirmed that the LSCI analysis of the developed smartphone-based multimodal rigid endoscopic device provides adequate blood flow imaging in living tissues.

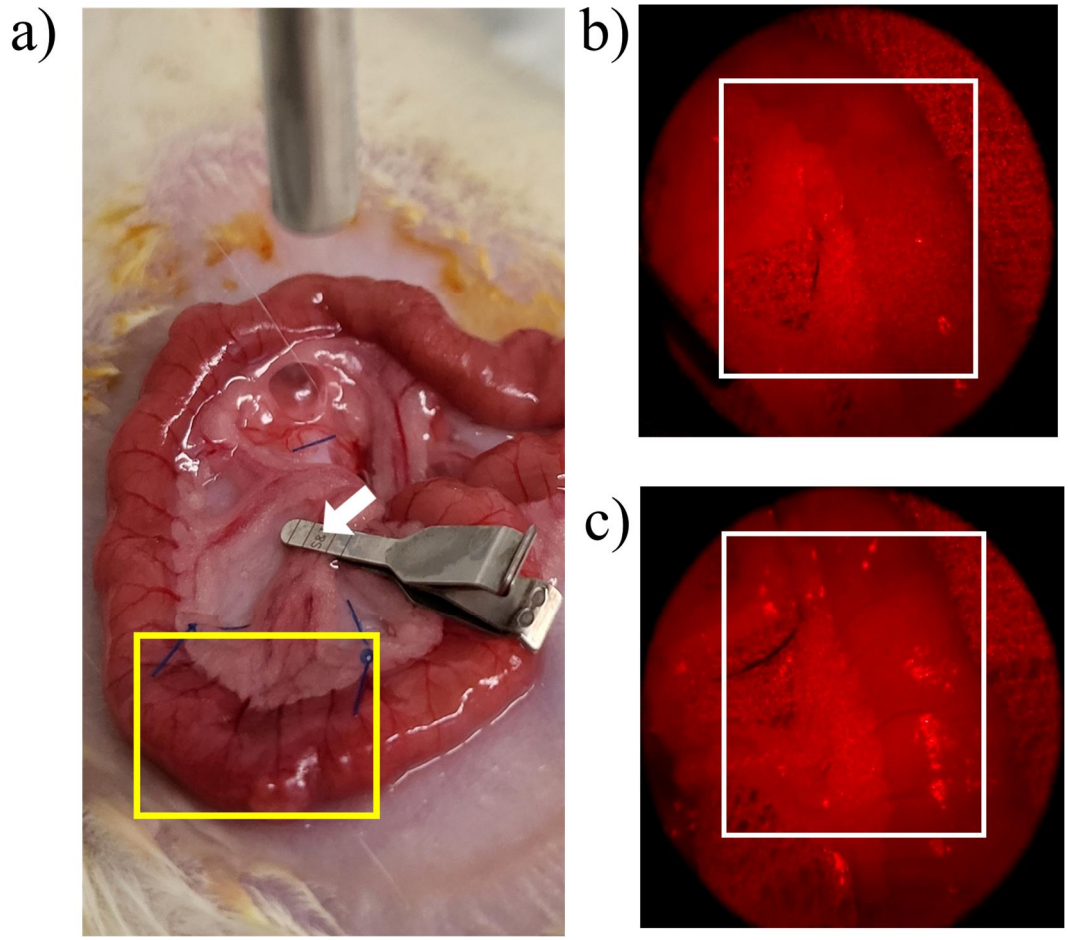

Figure 20. ***In vivo*** **rat ischemia experiment**

a) exposed rat small intestine for clamping the major arteries, b) 638nm raw speckle image at clamping situation, c) 638nm raw speckle image at declamping situation

An *in vivo* rat ischemia model experiment was conducted using the same method as the LSCI verification to confirm blood flow dynamics information acquisition using the RGB laser light source module. To obtain tissue oxygen saturation representing blood flow dynamics information, images were acquired using the 488nm laser and 638nm laser of the developed device's RGB laser light source module. Figure 22 a), b) and Figure 23 a), b) show the calculated and converted mapping images representing the time-dependent changes in tissue oxygen saturation based on the acquired image data. Figures 22 a) and b) show that when blood flow is blocked by clamping, tissue oxygen saturation gradually decreases in the area of interest below the edge vascular suture area marked with red arrows, similar to the LSCI results. This can be quantitatively confirmed in Figure 22 c), which represents the changes in average oxyhemoglobin, deoxyhemoglobin, and total hemoglobin concentrations in the red box area of Figure 22. b). It shows that tissue oxygen saturation drops as blood flow becomes interrupted over about 30 seconds. Figures 23. a) and b) show the changes in tissue oxygen saturation when blood flow is restored after 15 minutes of obstruction caused by clamping. It shows an increase in tissue oxygen saturation in the area of interest. Also, Figure 23. c) shows a rapid increase in tissue oxygen saturation when the blood flow is restored by releasing the clamp, as calculated from the changes in average oxyhemoglobin, deoxyhemoglobin, and total hemoglobin concentrations in the blue box area of Figure 23 b). The results are in Figure 22. and 23. demonstrate that the developed smartphone-based multimodal rigid endoscopic device can acquire blood flow dynamics images representing changes in tissue oxygen saturation.

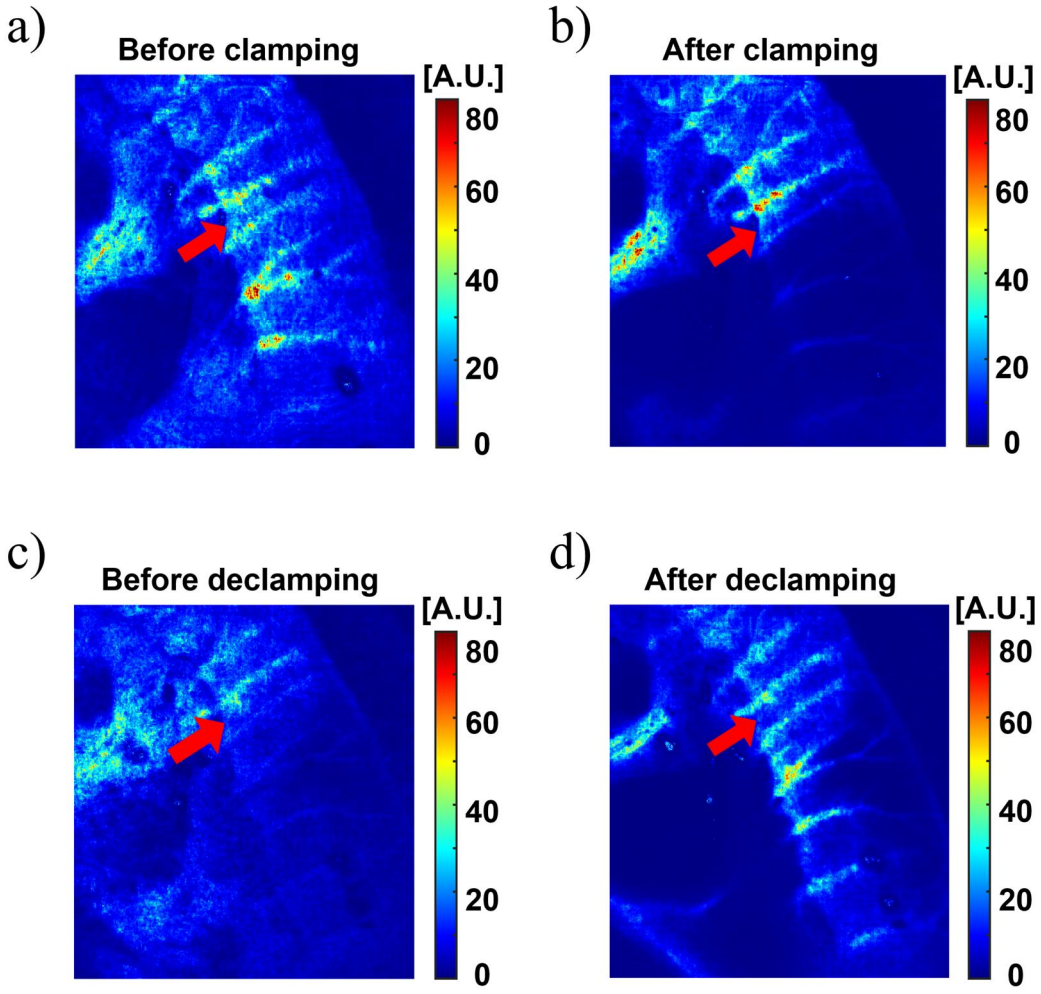

Figure 21. *In vivo*, rat ischemia experiment LSCI result.

a) Speckle Flow Index (SFI) mapping image before clamping, b) SFI mapping image after clamping, c) SFI mapping image before declamping, d) SFI mapping image after declamping.

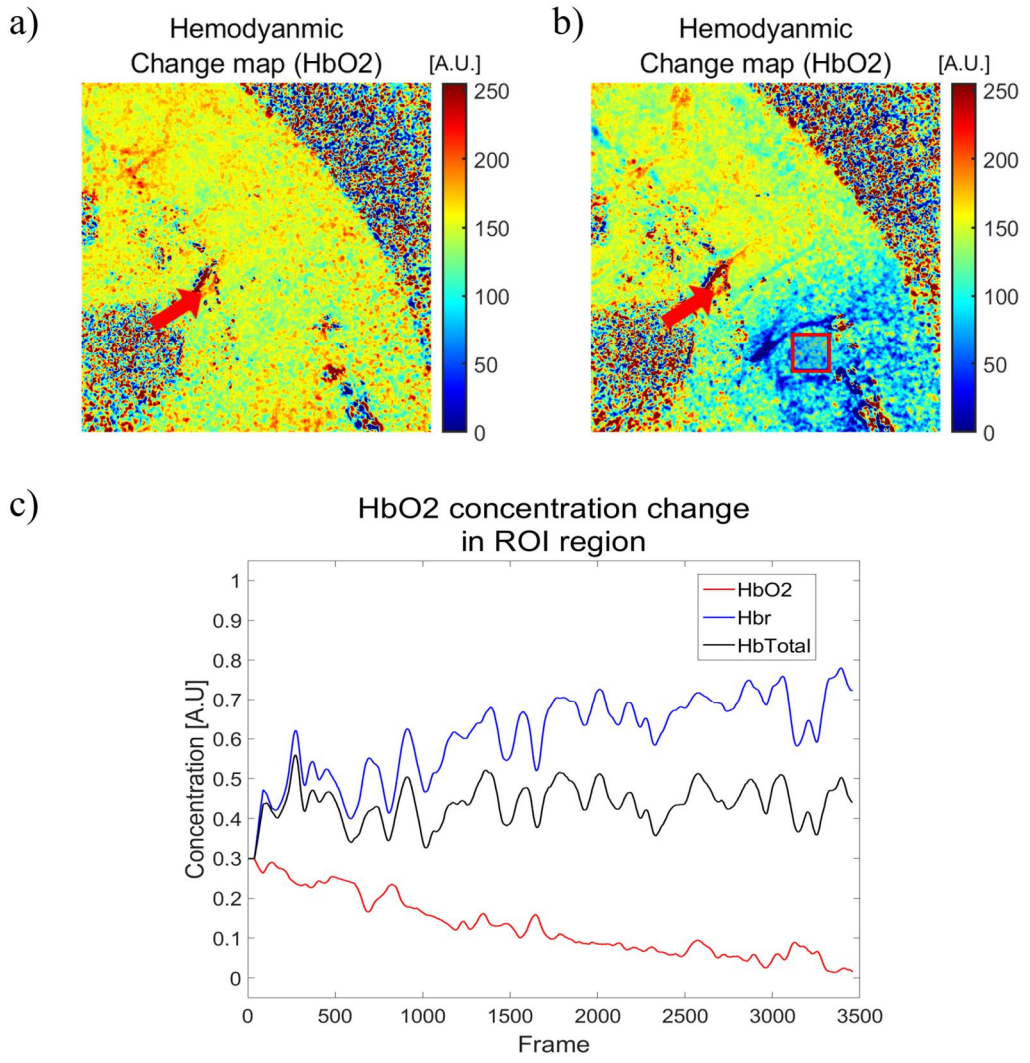

Figure 22. *In vivo* rat ischemia experiment hemodynamic result at clamping situation

a) Hemodynamic change mapping image with oxyhemoglobin concentration change before clamping, b) Hemodynamic change mapping image with oxyhemoglobin concentration change after clamping, c) oxyhemoglobin, deoxyhemoglobin, and total hemoglobin concentration change plot at ROI region at clamping situation.

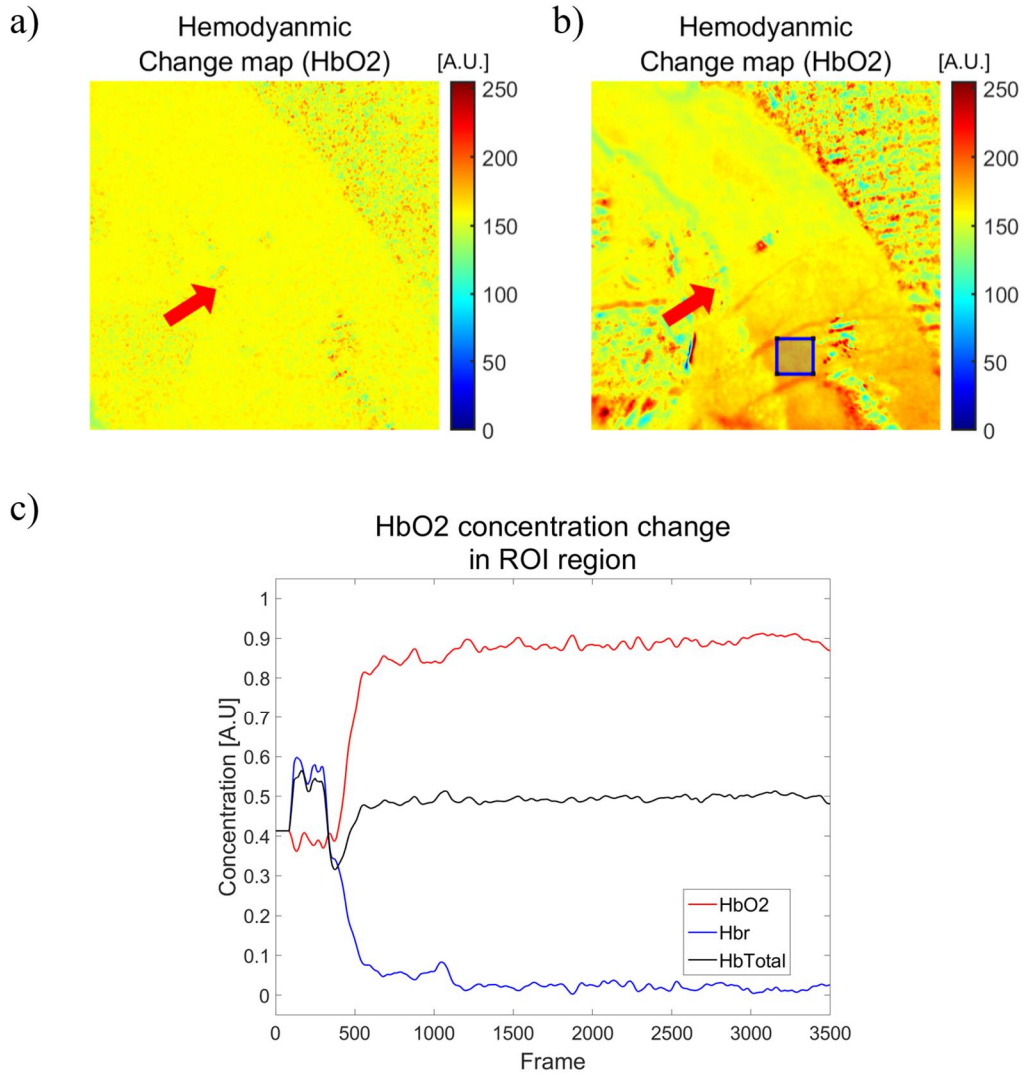

Figure 23. *In vivo* rat ischemia experiment hemodynamic result at declamping situation

a) Hemodynamic change mapping image with oxyhemoglobin concentration change before declamping recovery, b) Hemodynamic change mapping image with oxyhemoglobin concentration change after declamping recovery c) oxyhemoglobin, deoxyhemoglobin, and total hemoglobin concentration change plot at ROI region at declamping recovery situation

Conclusion

Building on previous research, this study aimed to extend the applicability of a smartphone-based endoscopic device as a Point of Care Testing (POCT) clinical diagnostic tool by incorporating additional functional imaging. We sought to analyze tissue oxygen saturation using Laser Speckle Contrast Imaging (LSCI) and dual-wavelength imaging, inspired by the combination of LSCI and hyperspectral imaging. However, given the complexity, lack of portability, and cost associated with hyperspectral imaging, we instead applied a dual-wavelength hemodynamic imaging analysis method to our smartphone-based endoscopic device,[82, 83, 85, 86] using an RGB laser module as the light source. This simplified, affordable system successfully acquired both LSCI data and tissue oxygen saturation change image data in phantom and in-vivo rat ischemia experiments. This portable smartphone endoscope system can observe the vascular flow and analyze tissue perfusion due to damage through hemodynamic response imaging. By integrating LSCI and multispectral imaging into a single device, we provide surgeons with real-time information on tissue health, enabling better-informed surgical decisions. The device's compact and low-cost design shows promise for wider healthcare applications, potentially improving surgical outcomes and reducing complications.

Discussion

Endoscopic imaging is one of the few means capable of optically transmitting images of internal organs in the human body, making it extremely important in the field of clinical diagnostics. [4, 6, 11, 87, 88] However, despite its role in clinical diagnostics, the use of endoscopy in the POCT (Point-of-Care Testing) field has been limited due to high costs and low portability of traditional endoscopic equipment. In the context of limited endoscopic use for POCT, smartphones emerged as the most notable devices in the field, rather than traditional clinical diagnostic equipment.[19, 21, 25, 89-91]

Smartphones have advanced at an astonishing pace due to the rapid growth of the semiconductor industry and competition among manufacturers. This advancement included not only the processing speeds but also the performance of built-in cameras and the number of environment-sensing sensors. Research on creating clinical diagnostic devices using these improved smartphones has been very active in the POCT field. The advantages of utilizing smartphones as POCT clinical diagnostic equipment ironically come from their widespread personal use and increased accessibility to patients.

Recent studies have announced that combining smartphones, with their increasing importance in the POCT field, with endoscopy, is an essential imaging equipment in clinical diagnostics.[29, 92-94] However, attempts to develop image diagnostic equipment by combining smartphones and endoscopy fell short of reflecting the improved performance of smartphone cameras and the combination of functional imaging in the field of endoscopic imaging. To address this shortfall, we developed a smartphone-based endoscopic device that applies high-speed video acquisition made possible by the enhanced performance of smartphone cameras and examined its potential for functional imaging analysis, rather than

just conventional endoscopic images, to evaluate the usability of the smartphone-based endoscopic device for POCT clinical diagnosis.

First, the research on the diagnosis of voice abnormalities using HSDI(high-speed digital imaging) of a smartphone-based endoscope started with the aim of verifying the diversification of utilization in clinical diagnosis using the high-performance camera function of the latest smartphones. We created a basic smartphone-based endoscopic device and used the high-speed video capture of the built-in smartphone cameras to diagnose voice disorders. The commercially available HSDI device is used for vocal cord function-related disease diagnosis in otolaryngology, but its high cost and additional equipment for image processing and transmission make it difficult to use in economically challenged countries. Additionally, it also faces difficulties in advanced medical facilities due to limited space. Therefore, the low-cost POCT device that can partially substitute for commercialized HSDI diagnostic equipment is highly applicable in clinical settings.

The developed smartphone-based endoscope device consists of a conventional endoscope, a personal smartphone, a 3D-printed adapter, and low-cost optical components, reducing costs and making procurement easier. Based on these advantages, the device was able to capture a vocal cord diagnostic image at 940 fps. To analyze the acquired video, the clinician first masked the glottal area and then divided and quantified the glottal area to calculate diagnostic reference values. The values calculated were the entire glottal area variation and the left and right glottal area variations, which were used to define basic phase and lateral phase differences in actual clinical diagnosis.

Using quantitative analysis data from healthy female participants as a basis for the control group, we were able to obtain the basic frequency of vocal cords of the subjects, which was 224Hz, similar to the average basic frequency of 217Hz for adult females.[61] Subsequent quantitative analyses of vocal cord disease patients showed that several clinical features that distinguish patients from healthy individuals were successfully obtained by comparing the patient analysis data with control group analysis data. As shown in Figure 6, all patient groups had limited vocal cord vibration amplitude as observed by quantitative analysis of glottal area variation data. The patient with left vocal cord palsy showed a significantly lower vibration amplitude in the left glottal area than in the right glottal area. Patients with chronic laryngitis exhibited an increased minimal vibration amplitude due to the limited closure of the glottal area, and the patient with right vocal polyps showed an imbalance between the left and right glottal area vibration amplitudes and an increase in minimal vibration amplitude. As a result, we were able to demonstrate the possibility of processing useful diagnostic reference values in the clinical images of healthy individuals and present the possibility of disease diagnosis for actual patients.

	Commercial HSDI system (FASTCAMMC2, Photron, Japan)	Smartphone-based endoscope HSDI system
Frame rate	4000 fps	940 fps
Pixel count	512 × 512	1280 × 720
Price	> $10,000,	< $500,
Weight	Total: 5,100 g	Total: 496 g

Table 1. Comparison between a commercial HSDI system and the developed smartphone-based endoscope HSDI system

While commercially available HSDI systems cost over $10,000 (as shown in Table 1), the smartphone-based endoscope HSDI device developed in this study can be assembled for less than $500. Furthermore, the smartphone-based endoscope HSDI device has a higher video resolution than commercialized HSDI devices, which can help identify details potentially useful for clinical diagnosis. However, due to its low cost and high portability, smartphone camera performance is lower than that of commercial HSDI systems, thus limiting its applicability. The frame rate of the smartphone camera's high-speed video performance is low, at 940 fps, compared to that of commercial HSDI systems, which require a minimum of 4000 fps to observe the detailed details of a single vibration cycle of the vocal cord. Additionally, high-power light source problems are also a limitation, due to the limitation of the acquisition time of smartphone cameras (up to 0.4 seconds) and relatively low sensitivity of CMOS sensors, requiring filtering in frequency analysis.

However, despite these limitations, we were able to demonstrate the potential of using smartphone-based endoscope HSDI devices for vocal cord diagnosis. Future improvements in smartphone camera capabilities and the use of AI-based image processing and deep learning can help overcome the limitations of the current technology, and additional upgrades to the smartphone and endoscope adapter can help expand its applicability beyond vocal cord function analysis to other clinical diagnostic areas as a POCT diagnostic device.

In the next study, to overcome the above limitations we developed an endoscopic system combined with smartphone cameras capable of acquiring laser speckle contrast imaging (LSCI) images. The developed system was designed to acquire both conventional endoscopic images and LSCI images using white LED and green laser. To verify blood flow in LSCI, a camera with a short exposure time of more than 100fps is required, rather than a conventional 30-

60fps video. Due to the rapid increase in the performance of current smartphones, it is now possible to shoot 120fps videos even in low-cost smartphones, which allowed us to attempt LSCI image acquisition using smartphone cameras. Despite LSCI's ability to provide more diverse biological imaging information by visualizing vessels and blood flow with a relatively simple system configuration, few attempts have been made to utilize it in clinical diagnosis and treatment domains. One notable application of LSCI in clinical diagnosis and treatment was its use in identifying porcine bowel vessels during laparoscopic surgery as a surgical auxiliary tool. [39] The limited clinical application is due to the need for additional equipment such as laser light sources, high-speed cameras, and image-processing PCs in existing LSCI endoscopic devices. Maintaining such LSCI configurations in POCT devices is also deemed unsuitable. In this study, we designed and fabricated an LSCI endoscopy system based on smartphones and verified its feasibility in acquiring biological LSCI data. We validated the LSCI image acquisition capability of the developed device through tissue-mimicking phantom experiments and *in vivo* experiments using rat models induced by BBN. The results of this study suggest the potential application of the system as a clinical diagnostic device for POCT in the future. The current developed system only acquires LSCI images using a single wavelength laser source; however, the design and fabrication process undertaken in this study confirms the possibility of providing a wider range of functional images by incorporating additional laser light source configurations.

In the previous study, the smartphone-based endoscopic device was developed to verify the feasibility of using the device as a POCT (Point of Care Testing) clinical diagnostic device and to increase its applicability as a POCT diagnostic device by adding functional imaging. In addition to LSCI (Laser Speckle Contrast Imaging) from the previous study, we aimed to enhance the possibility of its use as a POCT clinical diagnostic device by adding more functional imaging. Inspired by the combination of LSCI and hyperspectral imaging in

previous studies, in this study, we aimed to develop a smartphone-based endoscopic device capable of analyzing tissue oxygen saturation using LSCI and dual-wavelength imaging. [78, 82, 83, 95-102]

Although the existing hyperspectral imaging can accurately analyze and provide changes in tissue oxygen saturation, it requires special optical configurations or camera sensors to acquire hyperspectral images, which is not ideal for the simplicity, portability, and affordability of POCT devices. Therefore, we switched to a dual wavelength DRI (Diffuse Reflectance Imaging) analysis method and applied it to a smartphone-based endoscopic device. Dual-wavelength LSCI and DRI acquisition have already been used in benchtop formats for obtaining cerebral cortex blood flow and brain activation mapping in small animals. However, these previous studies used a complicated benchtop system structure that made portability impossible due to the equipment needed to separate the two-wavelength light sources. By applying an RGB laser module as the light source for a smartphone-based endoscopic device, we were able to create a more straightforward and affordable system.

The developed device has been proven to acquire both LSCI data and tissue oxygen saturation change image data through phantom and in-vivo rat ischemia experiments. The developed portable smartphone endoscope system can not only observe vascular flow in simulated internal organs via LSCI but also analyze tissue perfusion due to tissue damage through hemodynamic response imaging. The integration of LSCI and multispectral imaging into a single device promises to provide surgeons with real-time information on tissue health, allowing them to make better-informed decisions during the surgical process.[38, 81, 103] Furthermore, the device's compact and low-cost design which takes advantage of established rigid endoscopes and commodity smartphones, demonstrates the potential for making these

imaging modalities more accessible in a wide range of healthcare settings, benefiting patients in terms of improved surgical outcomes and reduced complications. The developed smartphone-based endoscope is expected to be useful in various fields for POCT devices, especially in remote areas and underdeveloped countries where access to medical facilities is limited.

However, the developed smartphone-based endoscope has some limitations that need to be addressed for widespread adoption as a POCT. One limitation is that only trained professionals can operate the endoscope since it requires direct insertion into the human body. There is a proposal to overcome these limitations by applying smartphone-based motorized endoscopy, which is being explored in ongoing research. Currently, the smartphone-based endoscopy system uses wireless, non-face-to-face controls and has been proven to minimize damage to internal organs.[104, 105] By applying smartphone-based motorized endoscopy and wireless control technology, researchers expect the smartphone-based endoscope can be further utilized in POCT clinical diagnosis.

Conclusion

In this study, we aimed to develop a smartphone-based Point-Of-Care Testing (POCT) device, specifically an imaging diagnostic device utilizing endoscopy and conducted three research stages. The first stage involved verifying the integration of basic smartphone cameras and endoscopic imaging to confirm the potential for clinical diagnosis. During this process, we acquired endoscopic images using the high-speed image acquisition function of the smartphone and identified abnormal vocal cord movement due to lesions that were difficult to diagnose with conventional endoscopic images, thereby providing more reliable evidence for its clinical applicability. Subsequently, in line with ongoing research on functional endoscopic imaging, we aimed to acquire functional images from the developed smartphone-integrated endoscope. We prioritized the development of a device capable of capturing Laser Speckle Contrast Imaging (LSCI) images. By introducing LED and single laser light sources to the flexible endoscope, we designed a device that could acquire both bright-field and LSCI images. We confirmed the feasibility of capturing blood flow change images using LSCI in smartphone-based endoscopic imaging through preclinical *in vivo* experiments.

Lastly, to create a smartphone-based endoscope device incorporating both LSCI and Intrinsic Signal Optical Imaging (ISOI), we utilized an RGB laser module and conducted further preclinical *in vivo* experiments. These experiments demonstrated the device's capability to acquire both LSCI blood flow change images and ISOI tissue oxygen saturation change images. Ultimately, the developed smartphone-based endoscope POCT device is expected to enable faster and more accurate diagnoses in clinical settings by providing not only morphological changes of internal organs but also functional images, allowing users to assess tissue damage and recovery levels.

References

1. Bush, R.B., et al., *Dr. Bozzini's Lichtleiter. A translation of his original article (1806).* Urology, 1974. **3**(1): p. 119-23.
2. Hirschowitz, B.I., et al., *Demonstration of a new gastroscope, the fiberscope.* Gastroenterology, 1958. **35**(1): p. 50; discussion 51-3.
3. De Groen, P.C., *History of the Endoscope [Scanning Our Past]*. Proceedings of the IEEE, 2017. **105**(10): p. 1987-1995.
4. Kuipers, E.J. and J. Haringsma, *Diagnostic and therapeutic endoscopy.* Journal of Surgical Oncology, 2005. **92**(3): p. 203-209.
5. Li, Z. and P.W.-Y. Chiu, *Robotic Endoscopy.* Visceral Medicine, 2018. **34**(1): p. 45-51.
6. Moses, F.M. and J.S. Lee, *Current GI Endoscope Disinfection and QA Practices.* Digestive Diseases and Sciences, 2004. **49**(11-12): p. 1791-1797.
7. Moura, D.T.H.d., H. Aihara, and C.C. Thompson, *Robotic-assisted surgical endoscopy: a new era for endoluminal therapies.* VideoGIE, 2019. **4**(9): p. 399-402.
8. Yamada, M., et al., *Development of a real-time endoscopic image diagnosis support system using deep learning technology in colonoscopy.* Scientific Reports, 2019. **9**(1).
9. van Rossum, P.S.N., et al., *Endoscopic biopsy and EUS for the detection of pathologic complete response after neoadjuvant chemoradiotherapy in esophageal cancer: a systematic review and meta-analysis.* Gastrointestinal Endoscopy, 2016. **83**(5): p. 866-879.
10. Gulati, S., et al., *The future of endoscopy: Advances in endoscopic image innovations.* Digestive Endoscopy, 2019. **32**(4): p. 512-522.
11. Boese, A., et al., *Endoscopic Imaging Technology Today.* Diagnostics, 2022. **12**(5).
12. Mooney, P.D., et al., *Su1450 Point of Care Testing for Adult Celiac Disease: A Novel Role in Endoscopy.* Gastroenterology, 2014. **146**(5).
13. St John, A. and C.P. Price, *Existing and Emerging Technologies for Point-of-Care Testing.* Clin Biochem Rev, 2014. **35**(3): p. 155-67.
14. Thapa, P., et al., *Field Portable Micro Endoscopy for In vivo Microscopy of Cancerous Tissue: A Point of Care Device*, in *Icol-2019*. 2021. p. 289-292.
15. Murray, M.J., *Endoscopy in Sharks.* Veterinary Clinics of North America: Exotic Animal Practice, 2010. **13**(2): p. 301-313.
16. Divers, S.J., et al., *Field endoscopy for identifying gender, reproductive stage and gonadal anomalies in free-ranging sturgeon (Scaphirhynchus) from the lower Mississippi River.* Journal of Applied Ichthyology, 2009. **25**: p. 68-74.
17. Kang, D., et al., *An Operable, Portable, and Disposable Ultrathin Endoscope for Evaluation of the Upper Gastrointestinal Tract.* Digestive Diseases and Sciences, 2019. **64**(7): p. 1901-1907.
18. Choi, J.H., *Comparison of a novel bedside portable endoscopy device with nasogastric aspiration for identifying upper gastrointestinal bleeding.* World Journal of Gastroenterology, 2014. **20**(25).
19. Zhang, D. and Q. Liu, *Biosensors and bioelectronics on smartphone for portable biochemical detection.* Biosensors and Bioelectronics, 2016. **75**: p. 273-284.
20. del Rosario, M., S. Redmond, and N. Lovell, *Tracking the Evolution of Smartphone Sensing for Monitoring Human Movement.* Sensors, 2015. **15**(8): p. 18901-18933.
21. Agu, E., et al., *The smartphone as a medical device: Assessing enablers, benefits and challenges*, in *2013 IEEE International Workshop of Internet-of-Things Networking and Control (IoT-NC)*. 2013. p. 48-52.
22. McCracken, K.E. and J.-Y. Yoon, *Recent approaches for optical smartphone sensing in resource-limited settings: a brief review.* Analytical Methods, 2016. **8**(36): p. 6591-6601.
23. Geng, Z., et al., *Recent Progress in Optical Biosensors Based on Smartphone Platforms.* Sensors, 2017. **17**(11).
24. Griffiths, A.D., et al., *Scalable visible light communications with a micro-LED array projector and high-speed smartphone camera.* Optics Express, 2019. **27**(11).
25. Xu, X., et al., *Advances in Smartphone-Based Point-of-Care Diagnostics.* Proceedings of the IEEE, 2015. **103**(2): p. 236-247.
26. Liu, J., et al., *Point-of-care testing based on smartphone: The current state-of-the-art (2017–2018).* Biosensors and Bioelectronics, 2019. **132**: p. 17-37.
27. Uthoff, R.D., et al., *Point-of-care, multispectral, smartphone-based dermascopes for dermal lesion screening and erythema monitoring.* Journal of Biomedical Optics, 2020. **25**(06).
28. Ding, H., et al., *Smartphone based multispectral imager and its potential for point-of-care testing.* The Analyst, 2019. **144**(14): p. 4380-4385.
29. Bae, J.K., et al., *Smartphone-Based Endoscope System for Advanced Point-of-Care Diagnostics: Feasibility Study.* JMIR mHealth and uHealth, 2017. **5**(7).
30. Guo, J., *Smartphone-Powered Electrochemical Dongle for Point-of-Care Monitoring of Blood β-Ketone.*

Analytical Chemistry, 2017. **89**(17): p. 8609-8613.
31. Zhang, X., et al. *A low-cost and smartphone-based laser speckle contrast imager for blood flow*. in *BIBE 2018; International Conference on Biological Information and Biomedical Engineering*. 2018. VDE.
32. Spigulis, J., et al., *Mobile phone based laser speckle contrast imager for assessment of skin blood flow*, in *Eighth International Conference on Advanced Optical Materials and Devices (AOMD-8)*. 2014.
33. Fercher, A.F. and J.D. Briers, *Flow visualization by means of single-exposure speckle photography.* Optics Communications, 1981. **37**(5): p. 326-330.
34. Boas, D.A. and A.K. Dunn, *Laser speckle contrast imaging in biomedical optics.* Journal of Biomedical Optics, 2010. **15**(1).
35. Briers, D., et al., *Laser speckle contrast imaging: theoretical and practical limitations.* Journal of Biomedical Optics, 2013. **18**(6).
36. Senarathna, J., et al., *Laser Speckle Contrast Imaging: Theory, Instrumentation and Applications.* IEEE Reviews in Biomedical Engineering, 2013. **6**: p. 99-110.
37. Miller, D.R., et al., *Continuous blood flow visualization with laser speckle contrast imaging during neurovascular surgery.* Neurophotonics, 2022. **9**(02).
38. Zheng, C., L.W. Lau, and J. Cha, *Dual-display laparoscopic laser speckle contrast imaging for real-time surgical assistance.* Biomedical Optics Express, 2018. **9**(12).
39. Wildeboer, A., et al., *Laparoscopic Laser Speckle Contrast Imaging Can Visualize Anastomotic Perfusion: A Demonstration in a Porcine Model.* Life, 2022. **12**(8).
40. Dunn, A.K., et al., *Simultaneous imaging of total cerebral hemoglobin concentration, oxygenation, and blood flow during functional activation.* Optics Letters, 2003. **28**(1).
41. Kim, E., E. Anguluan, and J.G. Kim, *Monitoring cerebral hemodynamic change during transcranial ultrasound stimulation using optical intrinsic signal imaging.* Scientific Reports, 2017. **7**(1).
42. Morone, K.A., et al., *Review of functional and clinical relevance of intrinsic signal optical imaging in human brain mapping.* Neurophotonics, 2017. **4**(3).
43. Gratzer, W.B. and G.H. Beaven, *Transparent starch gels: Preparation, optical properties and application to haemoglobin characterisation.* Clinica Chimica Acta, 1960. **5**(4): p. 577-582.
44. Townsend, D., Journal of Medical and Biological Engineering, 2014. **34**(2).
45. Soraya, G., et al., *A Label-Free, Quantitative Fecal Hemoglobin Detection Platform for Colorectal Cancer Screening.* Biosensors, 2017. **7**(4).
46. Banerjee, A., et al., *Non-invasive estimation of hemoglobin, bilirubin and oxygen saturation of neonates simultaneously using whole optical spectrum analysis at point of care.* Scientific Reports, 2023. **13**(1).
47. Eckle, T., et al., *Non-Invasive Measurement of Hemoglobin: Assessment of Two Different Point-of-Care Technologies.* PLoS ONE, 2012. **7**(1).
48. Hillman, E.M.C., *Optical brain imaging in vivo: techniques and applications from animal to man.* Journal of Biomedical Optics, 2007. **12**(5).
49. Ma, Y., et al., *Wide-field optical mapping of neural activity and brain haemodynamics: considerations and novel approaches.* Philosophical Transactions of the Royal Society B: Biological Sciences, 2016. **371**(1705).
50. Tank, A., et al., *Diffuse optical spectroscopic imaging reveals distinct early breast tumor hemodynamic responses to metronomic and maximum tolerated dose regimens.* Breast Cancer Research, 2020. **22**(1).
51. Mehta, D.D., et al., *Automated Measurement of Vocal Fold Vibratory Asymmetry From High-Speed Videoendoscopy Recordings.* Journal of Speech, Language, and Hearing Research, 2011. **54**(1): p. 47-54.
52. Deliyski, D.D., et al., *Clinical Implementation of Laryngeal High-Speed Videoendoscopy: Challenges and Evolution.* Folia Phoniatrica et Logopaedica, 2008. **60**(1): p. 33-44.
53. Eysholdt, U., et al., *Direct Evaluation of High-Speed Recordings of Vocal Fold Vibrations.* Folia Phoniatrica et Logopaedica, 1996. **48**(4): p. 163-170.
54. Wittenberg, T., et al., *Functional imaging of vocal fold vibration: Digital multislice high-speed kymography.* Journal of Voice, 2000. **14**(3): p. 422-442.
55. Hirose, H., *High-speed Digital Imaging of Vocal Fold Vibration.* Acta Oto-Laryngologica, 2009. **105**(sup458): p. 151-153.
56. Echternach, M., S. Dippold, and B. Richter, *High-speed imaging using rigid laryngoscopy for the analysis of register transitions in professional operatic tenors.* Logopedics Phoniatrics Vocology, 2014. **41**(1): p. 1-8.
57. Guzman, M., et al., *The influence of water resistance therapy on vocal fold vibration: a high-speed digital imaging study.* Logopedics Phoniatrics Vocology, 2016. **42**(3): p. 99-107.
58. Yamauchi, A., et al., *Quantification of Vocal Fold Vibration in Various Laryngeal Disorders Using High-Speed Digital Imaging.* Journal of Voice, 2016. **30**(2): p. 205-214.
59. Bohr, C., et al., *Quantitative analysis of organic vocal fold pathologies in females by high speed endoscopy.* The Laryngoscope, 2013. **123**(7): p. 1686-1693.
60. Poburka, B.J., R.R. Patel, and D.M. Bless, *Voice-Vibratory Assessment With Laryngeal Imaging (VALI) Form: Reliability of Rating Stroboscopy and High-speed Videoendoscopy.* Journal of Voice, 2017. **31**(4):

p. 513.e1-513.e14.
61. Huss, P.J., *Vocal Pitch Range and Habitual Pitch Level: The Study of Normal College Age Speakers*. 1983, Western Michigan University. p. 56.
62. Mirjalili, S., et al., *Influence of spatial camera resolution in high-speed videoendoscopy on laryngeal parameters.* Plos One, 2019. **14**(4).
63. Schlegel, P., et al., *Machine learning based identification of relevant parameters for functional voice disorders derived from endoscopic high-speed recordings.* Scientific Reports, 2020. **10**(1).
64. Kong, P., et al., *Laser Speckle Contrast Imaging Based on a Mobile Phone Camera.* Ieee Access, 2021. **9**: p. 76730-76737.
65. Richards, L.M., et al., *Low-cost laser speckle contrast imaging of blood flow using a webcam.* Biomedical Optics Express, 2013. **4**(10).
66. Patel, D.D. and D.M. Lipinski, *Validating a low-cost laser speckle contrast imaging system as a quantitative tool for assessing retinal vascular function.* Scientific Reports, 2020. **10**(1).
67. Qiu, J., *Spatiotemporal laser speckle contrast analysis for blood flow imaging with maximized speckle contrast.* Journal of Biomedical Optics, 2010. **15**(1).
68. Nordstrom, R.J., et al., *Fabrication and characterization of silicone-based tissue phantoms with tunable optical properties in the visible and near infrared domain*, in *Design and Performance Validation of Phantoms Used in Conjunction with Optical Measurements of Tissue*. 2008.
69. Raghavachari, R., et al., *Polydimethylsiloxane tissue-mimicking phantoms for quantitative optical medical imaging standards*, in *Design and Quality for Biomedical Technologies X*. 2017.
70. Goldfain, A.M., et al., *Polydimethylsiloxane tissue-mimicking phantoms with tunable optical properties.* Journal of Biomedical Optics, 2021. **27**(07).
71. Degoricija, M., et al., *The dynamics of the inflammatory response during BBN-induced bladder carcinogenesis in mice.* Journal of Translational Medicine, 2019. **17**(1).
72. Vasconcelos-Nobrega, C., et al., *Review: BBN as an urothelial carcinogen. In vivo*, 2012. **26**(4): p. 727-39.
73. White, S.M., et al., *Simultaneous Blood Flow Measurement and Dermoscopy of Skin Lesions Using Dual-Mode Dermascope.* Scientific Reports, 2018. **8**(1).
74. Heeman, W., et al., *Application of laser speckle contrast imaging in laparoscopic surgery.* Biomedical Optics Express, 2019. **10**(4).
75. Mennes, O.A., et al., *Assessment of microcirculation in the diabetic foot with laser speckle contrast imaging.* Physiological Measurement, 2019. **40**(6).
76. Heeman, W., et al., *Clinical applications of laser speckle contrast imaging: a review.* Journal of Biomedical Optics, 2019. **24**(08).
77. Kim, Y., et al., *Compact Smartphone-Based Laser Speckle Contrast Imaging Endoscope Device for Point-of-Care Blood Flow Monitoring.* Biosensors, 2022. **12**(6).
78. Chen, W., et al., *Cocaine-Induced Abnormal Cerebral Hemodynamic Responses to Forepaw Stimulation Assessed by Integrated Multi-Wavelength Spectroimaging and Laser Speckle Contrast Imaging.* IEEE Journal of Selected Topics in Quantum Electronics, 2016. **22**(4): p. 146-153.
79. Satat, G., et al., *Computational Laser Speckle Contrast Imaging in Endoscopic System*, in *Imaging and Applied Optics 2016*. 2016.
80. Patel, D.D., et al., *Development of a Preclinical Laser Speckle Contrast Imaging Instrument for Assessing Systemic and Retinal Vascular Function in Small Rodents.* Translational Vision Science & Technology, 2021. **10**(9).
81. Lee, S., et al., *Multimodal Imaging of Laser Speckle Contrast Imaging Combined With Mosaic Filter-Based Hyperspectral Imaging for Precise Surgical Guidance.* IEEE Transactions on Biomedical Engineering, 2022. **69**(1): p. 443-452.
82. Qin, J., et al., *Fast synchronized dual-wavelength laser speckle imaging system for monitoring hemodynamic changes in a stroke mouse model.* Optics Letters, 2012. **37**(19).
83. Luo, Z., et al., *Simultaneous imaging of cortical hemodynamics and blood oxygenation change during cerebral ischemia using dual-wavelength laser speckle contrast imaging.* Optics Letters, 2009. **34**(9).
84. Tumanov, A.V., et al., *Murine Model of Intestinal Ischemia-reperfusion Injury.* Journal of Visualized Experiments, 2016(111).
85. Shemesh, D., et al., *Decreased cerebral blood flow and hemodynamic parameters during acute hyperglycemia in mice model observed by dual wavelength speckle imaging.* Journal of Biophotonics, 2019. **12**(8).
86. Lee, S., et al., *Depth-dependent cerebral hemodynamic responses following Direct Cortical Electrical Stimulation (DCES) revealed by in vivo dual-optical imaging techniques.* Optics Express, 2012. **20**(7).
87. Davila, R.E., et al., *ASGE guideline: the role of endoscopy in the diagnosis, staging, and management of colorectal cancer.* Gastrointestinal Endoscopy, 2005. **61**(1): p. 1-7.
88. Rosen, C.A. and T. Murry, *Diagnostic Laryngeal Endoscopy.* Otolaryngologic Clinics of North America, 2000. **33**(4): p. 751-757.

89. Purohit, B., et al., *Smartphone-assisted personalized diagnostic devices and wearable sensors*. Current Opinion in Biomedical Engineering, 2020. **13**: p. 42-50.
90. Roda, A., et al., *Smartphone-based biosensors: A critical review and perspectives*. TrAC Trends in Analytical Chemistry, 2016. **79**: p. 317-325.
91. Chatzipapas, I., et al., *Using a Mobile Smartphone to Perform Laparoscopy.* Journal of Minimally Invasive Gynecology, 2018. **25**(5): p. 912-915.
92. Çelikoyar, M.M. and O.T. Aktas, *Endoscopy in otolaryngology utilising smartphone as the capturing device.* Journal of Visual Communication in Medicine, 2018. **41**(3): p. 118-121.
93. Alawsi, T. and Z. Al Bawi, *A review of smartphone point of care adapter design.* Engineering Reports, 2019. **1**(2).
94. Quimby, A.E., et al., *Smartphone adapters for flexible Nasolaryngoscopy: a systematic review.* Journal of Otolaryngology - Head & Neck Surgery, 2018. **47**(1).
95. Rege, A., et al., *In vivo laser speckle imaging reveals microvascular remodeling and hemodynamic changes during wound healing angiogenesis.* Angiogenesis, 2011. **15**(1): p. 87-98.
96. Jansen-Winkeln, B., et al., *Determination of the transection margin during colorectal resection with hyperspectral imaging (HSI).* International Journal of Colorectal Disease, 2019. **34**(4): p. 731-739.
97. Sicher, C., et al., *Hyperspectral imaging as a possible tool for visualization of changes in hemoglobin oxygenation in patients with deficient hemodynamics – proof of concept.* Biomedical Engineering / Biomedizinische Technik, 2018. **63**(5): p. 609-616.
98. Holmer, A., et al., *Hyperspectral imaging in perfusion and wound diagnostics – methods and algorithms for the determination of tissue parameters.* Biomedical Engineering / Biomedizinische Technik, 2018. **63**(5): p. 547-556.
99. Calin, M.A., et al., *Hyperspectral Imaging in the Medical Field: Present and Future.* Applied Spectroscopy Reviews, 2013. **49**(6): p. 435-447.
100. Wild, T., et al., *Hyperspectral imaging of tissue perfusion and oxygenation in wounds: assessing the impact of a micro capillary dressing.* Journal of Wound Care, 2018. **27**(1): p. 38-51.
101. Daeschlein, G., et al., *Hyperspectral imaging: innovative diagnostics to visualize hemodynamic effects of cold plasma in wound therapy.* Biomedical Engineering / Biomedizinische Technik, 2018. **63**(5): p. 603-608.
102. Lu, G. and B. Fei, *Medical hyperspectral imaging: a review.* Journal of Biomedical Optics, 2014. **19**(1).
103. Kojima, S., et al., *Laser Speckle Contrast Imaging for Intraoperative Quantitative Assessment of Intestinal Blood Perfusion During Colorectal Surgery: A Prospective Pilot Study.* Surgical Innovation, 2019. **26**(3): p. 293-301.
104. Moon, Y., et al., *Cost-Effective Smartphone-Based Articulable Endoscope Systems for Developing Countries: Instrument Validation Study.* JMIR mHealth and uHealth, 2020. **8**(9).
105. Moon, Y., et al., *A Wi-Fi–Based Mask-Type Laryngoscope for Telediagnosis During the COVID-19 Pandemic: Instrument Validation Study.* Journal of Medical Internet Research, 2021. **23**(10).

국문요약

임상 진단 영역에서 내시경은 인체의 다양한 내부 장기의 광학적 영상을 얻을 수 있는 유일무이 한 진단 장비이며 때문에 임상 영역에서 최초로 내시경이 도입된 이후 임상 진단에서의 중요성과 활용성이 내시경의 성능과 더불어 꾸준히 증가해 왔다. 이러한 내시경의 임상 중요성 때문에 의료 영역에서 주목받는 현장진단검사(POCT) 영역에서도 내시경을 적용하고자 하는 시도가 있었다. 또한 스마트폰은 자체 성능의 비약적인 발전과 그 휴대성과 보급률로 현장진단검사 영역에서는 가장 중요한 기기로 손꼽히고 있다. 위에서 언급한 내시경과 현장 진단검사의 융합에 스마트폰은 중요한 도구로 사용되고 있으며 본 연구에서도 스마트폰을 이용하여 내시경 영상을 획득하고 이를 진단영역에서 사용할 수 있는 가능성을 탐색하고자 하였다.

첫번째 연구에서는 성대 진동 후두 내시경영상을 스마트폰의 카메라를 이용하여 획득하고 이를 영상진단에 활용할 수 있는지를 알아보기 위하여 연구를 진행하였다. 성대의 진동 영상을 획득하기 위하여 스마트폰의 고속 촬영 기능을 활용 하였으며 자체 제작한 내시경 스마트폰 어댑터를 사용하여 정상인과 각기 다른 병변을 가진 4명의 환자를 대상으로 실제 임상 성대 진동영상을 획득 할 수 있었다. 획득한 임상 성대 진동 영상은 영상 처리 분석을 통해 정량화 하였고, 정량화된 변수들의 비교를 통해 정상인과 환자의 구별 뿐만 아니라 환자의 병변 간의 구분도 가능함을 밝혀냈다. 다음 연구에서는 기존 연구에서 밝혀낸 스마트폰을 이용한 내시경 영상의 임상진단 가능성을 더욱 높이기 위하여 단순한 명시야 내시경 영상이 아닌 기능적 영상을 통하여 생체조직의 다양한 정보를 추가적으로 얻고자 하였으며 이를 위해 사용한 것이 레이저 스페클 대조영상(LSCI) 분석 방법이다. LSCI를 구현 하기 위하여 추가적인 부품을 내장한 내시경 스마트폰 어댑터를 제작하고 이를 사용해 실제 LSCI 분석이 가능함을 생체 조직 모방 팬텀을 통해 검증하였다. LSCI 분석 검증을 완료한 장비를 실제 생체 내 영상에서도 사용이 가능함을 입증하기 위해 쥐의 방광 내 혈관 영상을 획득하였고 방광암 유발 쥐와 정상쥐 간의 혈관 영상과 그 차이를 LSCI를 통하여 나타낼 수 있었다. 마지막 후속 연구

로 기존 연구에서 개발된 LSCI의 분석 과 더불어 확산반사영상(DRI)를 획득하여 생체 조직의 혈류 흐름 뿐만 아니라 산소포화도 변화로 인한 조직 손상 가능성까지 확인 하고자 하였다. LSCI와 DRI를 모두 구현하기 위하여 RGB 레이저 모듈을 사용하였으며 기존의 LSCI검증 방식과 마찬가지로 생체조직모방팬텀을 사용해 LSCI 분석 능력을 검증하였으며, 이후 실제 쥐의 장간막 혈관 차단 실험을 통하여 DRI를 사용한 조직 산소포화도 영상 획득의 검증도 이루었다. LSCI와 DRI를 모두 스마트폰기반 내시경 장비에서 구현해 내면서 스마트폰 기반 내시경영상 장비가 실제 임상 현장 진단 영역에서 사용될 가능성을 더욱 높일 수 있었다.